npj | Computational Materials

www.nature.com/npjcompumats

REVIEW ARTICLE OPEN

Insights into the design of thermoelectric Mg_3Sb_2 and its analogs by combining theory and experiment

Jiawei Zhang[1], Lirong Song[1] and Bo Brummerstedt Iversen[1]

Over the past two decades, we have witnessed a strong interest in developing Mg_3Sb_2 and related $CaAl_2Si_2$-type materials for low- and intermediate-temperature thermoelectric applications. In this review, we discuss how computations coupled with experiments provide insights for understanding chemical bonding, electronic transport, point defects, thermal transport, and transport anisotropy in these materials. Based on the underlying insights, we examine design strategies to guide the further optimization and development of thermoelectric Mg_3Sb_2-based materials and their analogs. We begin with a general introduction of the Zintl concept for understanding bonding and properties and then reveal the breakdown of this concept in AMg_2X_2 with a nearly isotropic three-dimensional chemical bonding network. For electronic transport, we start from a simple yet powerful atomic orbital scheme of tuning orbital degeneracy for optimizing p-type electrical properties, then discuss the complex Fermi surface aided by high valley degeneracy, carrier pocket anisotropy, and light conductivity effective mass responsible for the exceptional n-type transport properties, and finally address the defect-controlled carrier density in relation to the electronegativity and bonding character. Regarding thermal transport, we discuss the insight into the origin of the intrinsically low lattice thermal conductivity in Mg_3Sb_2. Furthermore, the anisotropies in electronic and thermal transport properties are discussed in relation to crystal orbitals and chemical bonding. Finally, some specific challenges and perspectives on how to make further developments are presented.

npj Computational Materials (2019)5:76 ; https://doi.org/10.1038/s41524-019-0215-y

INTRODUCTION

The increasing energy consumption worldwide pushes significant efforts in developing alternative energy technologies. Thermoelectric (TE) technology, capable of converting waste heat into electrical energy, shows potential for waste heat-harvesting applications with a great advantage that TE devices are entirely in solid state with no moving parts, compact, quiet, and maintenance free.[1,2] One key bottleneck of this promising technology is its low conversion efficiency, which is essentially limited by low-performing materials. The performance of a TE material can be characterized by the dimensionless figure of merit, $zT = \alpha^2\sigma T/(\kappa_L + \kappa_e)$, where α is the Seebeck coefficient, σ is the electrical conductivity, T is the absolute temperature, κ_L is the lattice thermal conductivity, and the electronic thermal conductivity κ_e is related to σ through the Wiedemann–Franz law $\kappa_e = L\sigma T$ (L denotes the Lorenz number). The interdependent correlation among the TE transport parameters invokes numerous efforts[3–10] worldwide on decoupling these parameters so as to improve zT. In general, achieving a superior zT requires a combined effort of improving the power factor $\alpha^2\sigma$ and reducing the lattice thermal conductivity.

AB_2X_2 compounds with the $CaAl_2Si_2$-type structure, usually described as Zintl phases, are well recognized due to their promising TE properties. In these compounds, A is an alkaline earth or a divalent rare earth element, B is a transition metal or a main group element, and X usually comes from group 14, 15, or occasionally group 13.[11,12] The rich variety of compositions covered by AB_2X_2 ($CaAl_2Si_2$-type) compounds enables considerable chemical tunability of the electronic and thermal transport properties. During the past two decades, both theoretical and experimental aspects in $CaAl_2Si_2$-type TE materials have undergone a rapid development,[13–52] which results in a significant improvement of zT above unity (Fig. 1). Experimentally, strategies such as doping,[45–47,49,50] alloying,[15,16,18,19,21,23,25,29,35,36] and controlling vacancy concentrations[27] have been used to optimize electrical transport properties and to reduce thermal conductivity through point defect scattering. As nearly all these compounds are persistently p-type, it is a remarkable breakthrough that the low-cost Te-doped Mg_3Sb_2-based compounds were recently discovered to show exceptional n-type TE properties at low and intermediate temperatures (Fig. 1),[53–55] comparable or even superior to the commercial n-type TE materials, such as Bi_2Te_3 and PbTe. Hence, significant research efforts[56–73] on this promising material system are currently ongoing. Theoretically, electronic structures,[20,74–77] chemical bonding,[11,12,78,79] defects,[55,60,61,80] and phonon-related properties[81–84] have been extensively studied to understand the transport properties. The interplay between theory and experiment has given rise to many important guidelines based on the underlying physical and chemical insights for optimizing $CaAl_2Si_2$-type TEs.

In this review, we summarize some of the successful guiding principles for understanding and rationalizing the electrical and thermal transport in Mg_3Sb_2 and its derivatives with the $CaAl_2Si_2$-type structure. We show how computational efforts integrated with experiments lead to additional physical and chemical insights for the profound understanding of chemical bonding, electronic transport, defect chemistry, phonon transport, and transport anisotropy. We start from general introductions of crystal structure

[1]Center for Materials Crystallography, Department of Chemistry and iNANO, Aarhus University, 8000 Aarhus, Denmark
Correspondence: Bo Brummerstedt Iversen (bo@chem.au.dk)

Received: 19 February 2019 Accepted: 26 June 2019
Published online: 17 July 2019

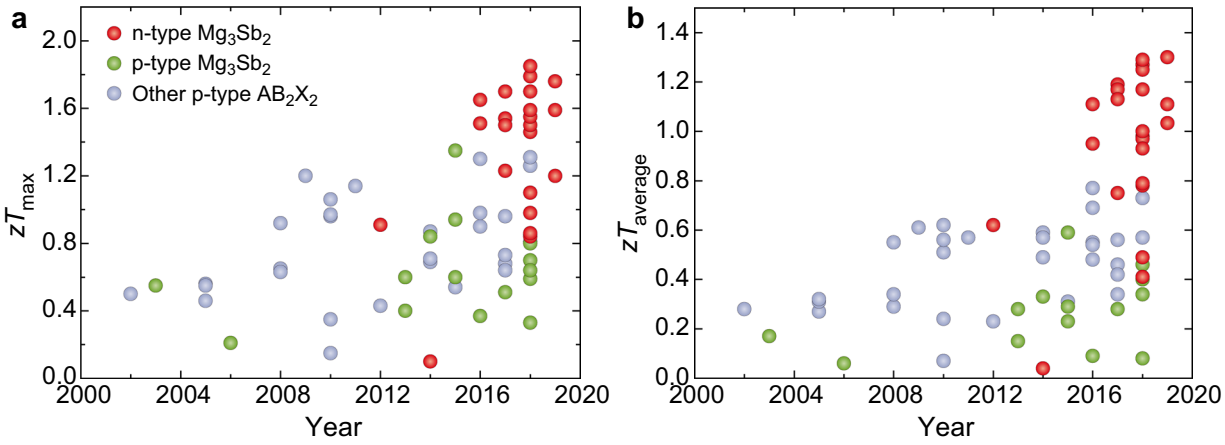

Fig. 1 **a**, **b** Timelines of **a** the maximum *zT* and **b** the average *zT* values of the reported AB_2X_2 thermoelectric materials with the $CaAl_2Si_2$-type structure. The average *zT* is calculated by the direct integration method within the entire measurement temperature range. The experimental data are taken from refs. [14–71]

and the Zintl concept that has been widely applied to understand the structure, bonding, and electronic transport in $CaAl_2Si_2$-type compounds. After that, we reveal the nearly isotropic three-dimensional (3D) chemical bonding network in AMg_2X_2, where the Zintl formalism is no longer applicable. For p-type electronic transport, we discuss how electronic transport can be optimized by minimizing the crystal orbital splitting energy via forming solid solutions and tuning biaxial strains, whereas for n-type transport we reveal the multi-valley conduction bands and complex Fermi surface as the electronic origin of the extraordinary n-type TE properties. Then we review the defect chemistry of the intrinsic p-type behavior and the surprising n-type behavior under different thermodynamic states, followed by highlighting the defect-controlled carrier transport and its correlation with the electronegativity and bonding character. For thermal transport, we review the studies on exploring the origin of the intrinsically low lattice thermal conductivity in Mg_3Sb_2 from first principles calculations. Moreover, we discuss the anisotropy in electrical and thermal transport properties with respect to crystal orbitals and chemical bonding. Finally, we conclude with some current challenges and prospects for future development.

CRYSTAL STRUCTURE

AB_2X_2 compounds with the trigonal $CaAl_2Si_2$-type structure[85] (space group: $P\bar{3}m1$) can be viewed as the $A^{\delta+}$ cationic layers intercalated between the tightly bound $[B_2X_2]^{\delta-}$ anionic layers (Fig. 2a). The three types of atoms A, B, and X occupy three different crystallographic sites 1a (0, 0, 0), 2d (1/3, 2/3, z_B), and 2d (1/3, 2/3, z_X) with point symmetries of $\bar{3}m$, $3m$, and $3m$, respectively. In the $[B_2X_2]^{\delta-}$ networks, B has a normal tetrahedral coordination, while X shows a unique distorted umbrella-like local environment.[12] As a result, the vertical B-X bond (d_3) along the *c* axis is usually longer than the three symmetry-equivalent tilted B-X bonds (d_2). Taking into account the cationic $A^{\delta+}$ layers, the interlayer A-X bonds (d_1) hold together the alternating cationic and anionic layers. Unlike the B atoms being tetrahedrally coordinated by the X atoms, each A atom occupies the octahedral site with six equal adjacent bonds. Each X atom, surrounded by four B atoms and three A atoms, has seven adjacent bonds including one vertical B-X bond, three tilted B-X bonds, and three interlayer A-X bonds (Fig. 2c–e).

Mg_3X_2 (X = As, Sb, and Bi) crystallizing in the inverse α-La_2O_3 structure is a special case of the $CaAl_2Si_2$ (AB_2X_2) structure with A and B being, respectively, Mg1 and Mg2.[86] The crystal structures of Mg_3Sb_2 and Mg_3Bi_2 were reported by Zintl and Husemann in 1933,[87] much earlier than those of ternary derivatives. From the reported phase diagram,[88,89] Mg_3Sb_2 and Mg_3Bi_2 show a phase transition from the low-temperature α phase to the high-temperature β phase at ~900 and ~700 °C, respectively. The high-temperature β phase is superionic with liquid-like magnesium ions and it is assumed to have a cubic structure,[90] but the exact crystal structure remains unclear.

ZINTL FORMALISM

The Zintl concept[91,92] plays a vital role in understanding structure, chemical bonding, and properties of a wide range of solid-state materials. Within this simple but powerful concept, the mostly ionic cations are considered merely as electron donors, donating their electrons to the covalently bonded anionic substructures. The covalent bonding in the anionic substructures ensures a significant orbital overlap, a light band mass, and thereby a high carrier mobility, whereas the ionic cations are suitable for doping with the aim to tune the carrier density without affecting the covalent anionic networks.[93,94] Such bonding features, as well as ideal band gaps, make charge-balanced Zintl compounds very promising for TE applications.

As described by Hoffmann et al.,[11,12] AB_2X_2 compounds with the $CaAl_2Si_2$-type structure can easily be understood as Zintl phases, where the covalently bonded $[B_2X_2]^{\delta-}$ layers receive electrons from the ionic $A^{\delta+}$ layers. Based on the aforementioned Zintl concept, considerable efforts have been made to explore AB_2X_2-type TE compounds and optimize them via doping, substituting, or creating vacancies on the cationic A sites. One notable example can be seen in $Ca_{1-x}Yb_xZn_2Sb_2$ alloys reported by Gascoin et al.,[15] which show the fine tunability of the carrier concentration through doping or substituting Ca with Yb. The alloying of Ca and Yb indeed has a negligible effect on the covalent anionic $[Zn_2Sb_2]^{2-}$ networks, so that the good carrier mobility and ideal energy gap are maintained. In addition, this alloying creates disorder in the cationic layers, which results in a reduction in thermal conductivity and an enhancement in *zT*.[15] Ever since this early work, the Zintl formalism has been broadly applied in developing and optimizing TE AZn_2Sb_2, ACd_2Sb_2, and their alloys.[20,23,27,32] In these compounds, however, it was found that the hole mobility may be greatly affected by changing the cation A from alkaline earth elements to rare earth elements.[20] Different synthesis methods were also found to result in a great change in carrier mobility of AZn_2Sb_2.[95] These results are likely induced by the change in carrier scattering time τ because the

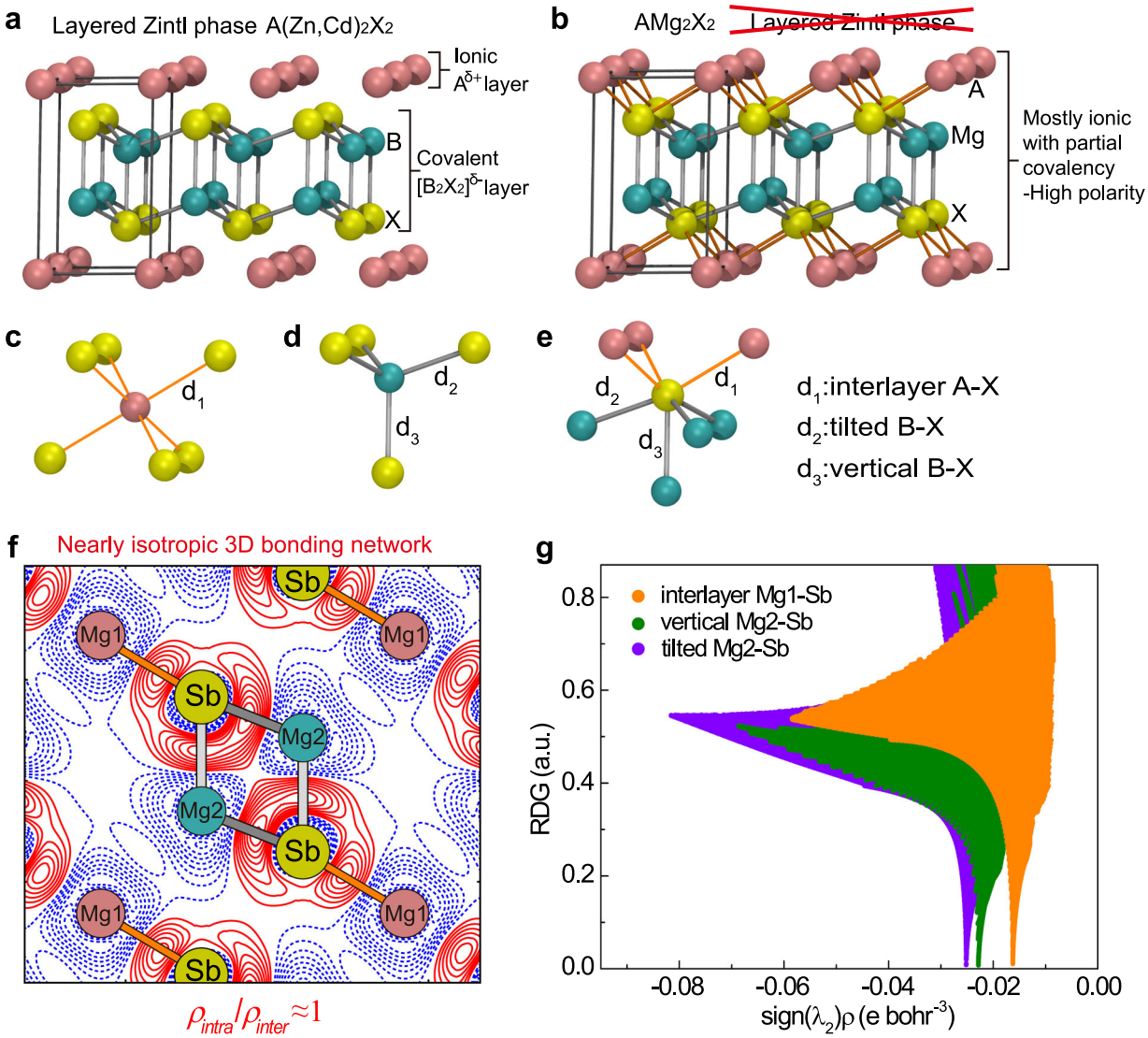

Fig. 2 **a** Crystal structure of layered Zintl phases $A(Zn,Cd)_2Sb_2$ with the $CaAl_2Si_2$-type structure, showing a clear distinction between the ionic $A^{\delta+}$ layer and the covalent $[B_2X_2]^{\delta-}$ layer. **b** A more accurate structural view of AMg_2X_2 with the $CaAl_2Si_2$-type structure, which shows comparable interlayer and intralayer bonds being mostly ionic with partial covalent nature (high polarity). **c**–**e** Coordination environments of the three nonequivalent atoms **c** A, **d** B, and **e** X in AB_2X_2 compounds with the $CaAl_2Si_2$-type structure. **f** Static deformation electron density map on (110) plane of Mg_3Sb_2 with a nearly isotropic three-dimensional bonding network ($\rho_{intra}/\rho_{inter} \approx 1$). The contour interval is 0.006 e Å^{-3}. Positive (negative) contours are plotted with red solid (blue dotted) lines. **g** Noncovalent interaction analysis with reduced density gradient as a function of sign(λ_2)ρ for the interlayer and intralayer interactions in Mg_3Sb_2. sign(λ_2) is the sign of the second eigenvalue of the electron density Hessian matrix.[101] Figure is reproduced with permission from ref. [79], CC-BY-4.0

effective mass of the valence band is shown to be unaffected by varying the cation A.[20]

NEARLY ISOTROPIC 3D BONDING NETWORK IN AMG_2X_2: BREAKDOWN OF THE ZINTL FORMALISM

Despite being very successful in rationalizing the electronic transport, the Zintl formalism and electron counting are not universal and can only provide a qualitative insight. It does not give us any indications of the site preference, bond length difference in anionic networks, or the reason why intrinsic p-type Mg_3Sb_2 shows very poor carrier mobility. More accurate theoretical calculations based on quantum mechanics or density functional theory (DFT) are required to understand the structure and chemical bonding.

Using the crystal orbital overlap population approach based on the extended Hückel calculations, Hoffmann et al.[12] gave a rational explanation for the unusual umbrella-like local coordination environment of the anionic X atom and the bond length difference in the $[B_2X_2]^{\delta-}$ networks of the $CaAl_2Si_2$ (AB_2X_2) structure through making and breaking chemical bonds. In addition, they compared the local and extended constructions of the bonding in transition metal $CaAl_2Si_2$-type compounds with those in $ThCr_2Si_2$-type compounds and explained why compounds with the B-site elements being occupied by transition metals with the d^0, d^5, and d^{10} configurations only form the $CaAl_2Si_2$-type structure.[11] Burdett and Miller also conducted extended Hückel calculations to reveal the formalism of the Al_2Si_2 fragment in the $CaAl_2Si_2$-type structure and extended the fragment formalism to several other main group compounds.[77] The above studies were conducted only based on the chemical bonds in the $[B_2X_2]^{\delta-}$ networks, neglecting the effect of the cationic $A^{\delta+}$ layer. The contribution of the cationic Ca^{2+} layer to the chemical bonding and electronic structure of $CaAl_2Si_2$ was

Table 1. Bader atomic charge Q, the degree of ionicity, and $\rho_{intra}/\rho_{inter}$ of several AB_2X_2 compounds with the $CaAl_2Si_2$-type structure

Compounds	$\rho_{intra}/\rho_{inter}$	Q (e)			Degree of ionicity (%)	
		A	B	X	A layer	B_2X_2 layer
Mg_3Sb_2	1.47	1.51	1.47	−2.23	75.5	73.9
Mg_3Bi_2	1.38	1.43	1.40	−2.11	71.5	70.2
$CaMg_2Sb_2$	1.39	1.39	1.48	−2.17	69.5	73.2
$CaMg_2Bi_2$	1.37	1.37	1.42	−2.10	68.5	70.5
$CaZn_2Sb_2$	2.34	1.37	0.31	−0.99	68.5	24.3
$CaCd_2Sb_2$	2.20	1.38	0.28	−0.97	69.0	23.2

The data of Bader atomic charge and $\rho_{intra}/\rho_{inter}$ are adapted from ref. [79]. The degree of ionicity is estimated from the charge transfer index,[99] which is calculated by the average of the atomic charge divided by the nominal oxidation charge of the atoms in unit cell. ρ_{inter} denotes the electron density value at bond critical point (BCP) of the interlayer A-X bond, while ρ_{intra} represents the average electron density value at BCPs of the two intralayer B-X bonds. The data of $CaCd_2Sb_2$ are calculated in this work using the previous computational methods[79]

investigated by Alemany et al. using DFT calculations.[95] They found that the cationic layers show an important contribution to the covalent bonding of $CaAl_2Si_2$, although the cationic layers do not play a dominant role in the electronic structure and the origin of the conductivity behavior. In addition to these significant studies[11,12,78,96] on rationalizing structural formation and electronic structure using the molecular orbital approaches, Grin et al.[18] studied the chemical bonding in $YbCd_2Sb_2$ using the electron localizability indicator and showed that four-center bonding exists in this compound and the whole bonding picture can be described by the closed-shell configuration $[Yb^{2+}][Cd^{2+}]_2[Sb^{3-}]_2$. Based on the analysis of the electron density difference, Toberer et al.[20] discussed the chemical bonding in AZn_2Sb_2 (A = Sr, Ca, and Yb) and revealed the largely covalent nature of the Zn-Sb bonds as well as the charge accumulation from Sb to A. The A-Sb bond was found to be very asymmetric and slightly larger in $YbZn_2Sb_2$ than in $SrZn_2Sb_2$ or $CaZn_2Sb_2$, which might be attributed to the less electron transfer from the cation A to the anionic Zn_2Sb_2 slabs induced by the larger electronegativity of Yb in comparison to Sr or Ca.[20] Using DFT calculations, Li et al. revealed a much lower shear strength in Mg_3Sb_2 compared to $CaMg_2Sb_2$ and $CaZn_2Sb_2$, which was explained by the weaker interlayer Mg-Sb bond in Mg_3Sb_2.[97] Despite significant efforts on understanding chemical bonding, most of these efforts are qualitative and there is clearly a lack of a quantitative chemical bonding description of $CaAl_2Si_2$-type compounds based on topological analysis of the electron density.

Recent theoretical calculations extend our knowledge of chemical bonding in $CaAl_2Si_2$-type compounds. Quantitative analysis of full DFT electron density by Zhang et al.[79] elucidated that the Zintl formalism is perfectly applicable in AZn_2Sb_2 and ACd_2Sb_2 but not in AMg_2X_2 (including Mg_3X_2). The analysis was conducted using the quantum theory of atoms in molecules (QTAIM) developed by Bader.[98] QTAIM is based on the analysis of critical points of the electron density ρ, which are the points satisfying $\nabla\rho = 0$. The readers are referred to ref. [98] for the details of the method. The idea is clearly proved by the result of Bader atomic charges (see Table 1). In $CaZn_2Sb_2$ and $CaCd_2Sb_2$, the cationic and anionic layers show a remarkable difference in the degree of ionicity[99] estimated from atomic charges, i.e., the cationic layers are largely ionic while the anionic layers are mostly covalent. In contrast, nearly complete charge transfers are observed for all atoms in AMg_2X_2, which elucidates the mostly ionic nature in both cationic and anionic layers. This indicates that any description of AMg_2X_2, especially Mg_3Sb_2, as layered Zintl phases in all previous literature is incorrect.

Chemical bonds in AB_2X_2 ($CaAl_2Si_2$-type) compounds can be described as polar bonds based on the topological properties of the bond critical points (BCPs) using the classification scheme by Gatti.[100] The covalency of the intralayer bonds in the B_2X_2 networks, however, may vary a lot among different compounds. The intralayer B-X bonds are much more covalent and stronger than the mostly ionic interlayer A-X bonds in AZn_2Sb_2 and ACd_2Sb_2, whereas the intralayer bonds in AMg_2X_2 are only slightly stronger than the largely ionic interlayer bonds (see Table 1 and Fig. 2a, b, f). This is further confirmed by the similar reduced density gradient distributions of the three nonequivalent bonds from the non-covalent interaction analysis[101] in Mg_3Sb_2 (Fig. 2g). The chemical bonding analysis may be conducive to understanding transport properties. The mostly ionic feature with partial covalency (high polarity) of chemical bonds explains the intrinsically low carrier mobility[36,102] in p-type Mg_3Sb_2 and $CaMg_2Sb_2$. However, the high carrier mobility in AMg_2Bi_2 (A = Mg, Ca, Eu, and Yb)[26,41] cannot be understood from chemical bonding, though it could be attributed to the bipolar effect or the change in carrier scattering time induced by defects.

The electron density ratio $\rho_{intra}/\rho_{inter}$ is devised as a simplified parameter measuring the degree of anisotropy of the chemical bonding network in the Mg_3Sb_2-related structures,[79] where ρ_{intra} and ρ_{inter} represent the electron density values at BCPs of the intralayer and interlayer bonds, respectively. Unlike AZn_2Sb_2 and ACd_2Sb_2 with clear anisotropic chemical bonding networks ($\rho_{intra}/\rho_{inter}>2$), the AMg_2X_2 compounds show nearly isotropic 3D chemical bonding networks with $\rho_{intra}/\rho_{inter}$ typically being smaller than 1.5 and often close to unity (Table 1). The nearly isotropic 3D bonding networks can be used to understand the nearly isotropic structural and thermal properties especially lattice thermal conductivities in AMg_2X_2,[79] which will be discussed later.

CRYSTAL FIELD ORBITAL SPLITTING, ORBITAL DEGENERACY, AND P-TYPE ELECTRONIC TRANSPORT

In principle, the intrinsic electronic transport of a material is determined almost exclusively by the degeneracy and curvature of the electronic bands at the band edges. The Seebeck coefficient is typically determined by the density of states effective mass $m_d^* = N_v^{2/3} m_s^*$,[1,103] where N_v represents the valley degeneracy of the electronic bands and m_s^* denotes the effective mass of a single valley. As proposed by Goldsmid,[1,103] the optimum electrical transport performance can be expressed as being proportional to the weighted mobility $\mu(m_d^*/m_e)^{3/2}$, where μ and m_e represent the carrier mobility and the mass of an electron, respectively. Considering the case with predominant acoustic phonon scattering or alloy scattering, the weighted mobility can be simplified and written as N_v/m_c^* (N_v/m_s^* for an isotropic band), where m_c^* is the conductivity effective mass. It is clear that excellent electrical performance requires a high valley degeneracy as well as a light conductivity effective mass. Increasing valley degeneracy (including orbital degeneracy) has long been recognized as an efficient way to improve electrical transport performance through enhancing the Seebeck coefficient without explicitly decreasing the carrier mobility when the intervalley scattering is insignificant.[4,6,9,103,104] Below we will introduce how electrical transport can be rationalized through enhancing orbital degeneracy via minimizing the orbital splitting energy[105] in p-type AB_2X_2 compounds with the $CaAl_2Si_2$-type structure.

In $CaAl_2Si_2$-type compounds, the valence band maximum (VBM) located at the Γ point shows p orbital characteristics of the anions (Fig. 3a, b). Unlike the triply degenerate p orbitals at the Γ point in cubic structures protected by the point symmetry, the p_z orbital, due to the crystal field effect, is usually well separated from the p_x,

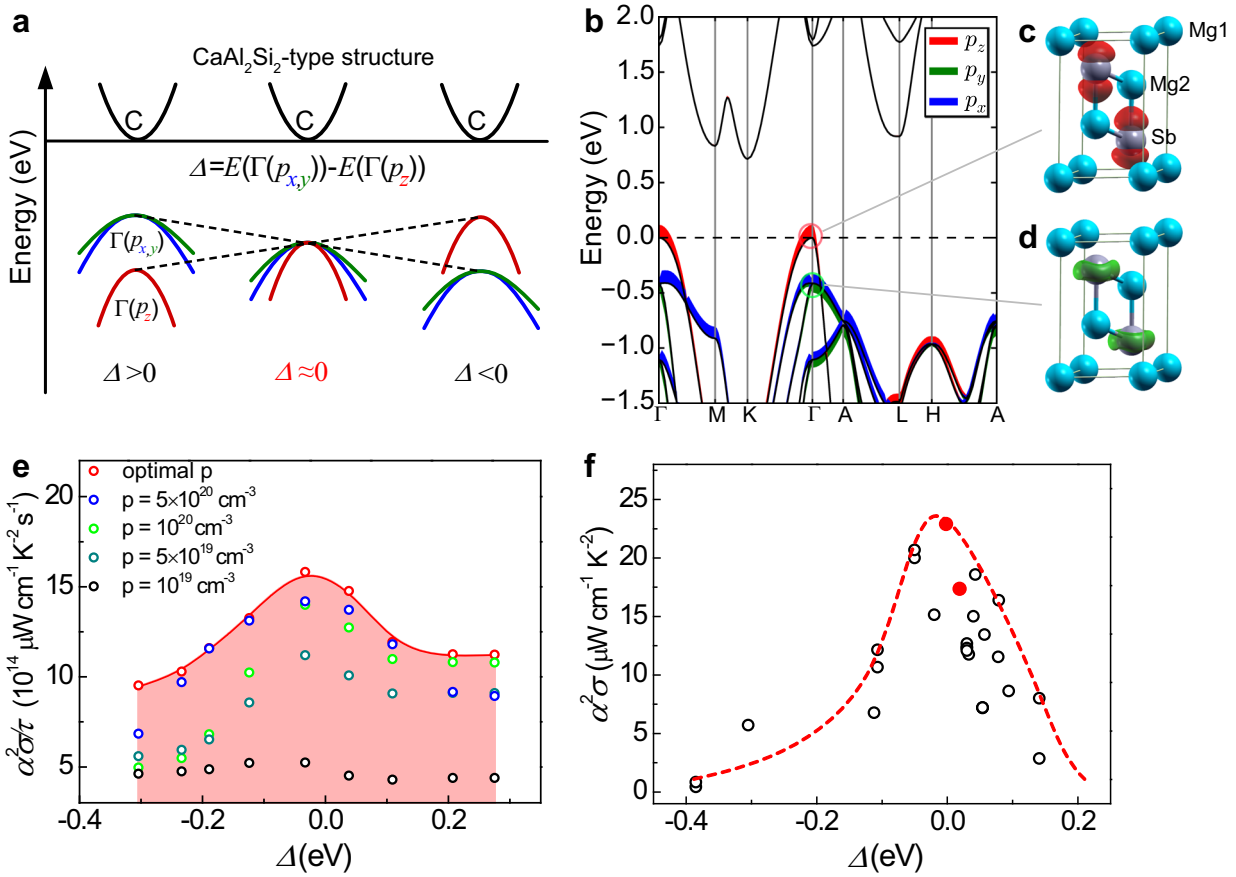

Fig. 3 **a** Schematic diagram of orbital engineering to realize three-fold degenerate *p* orbitals in $CaAl_2Si_2$-type compounds. Nondegenerate band $\Gamma(p_z)$ and doubly degenerate band $\Gamma(p_{x,y})$ are mainly composed of p_z and $p_{x,y}$ orbitals from the anions, respectively. Δ denotes the crystal field splitting energy between $p_{x,y}$ and p_z orbitals at the Γ point. **b** Band structure of Mg_3Sb_2 by TB-mBJ potential without spin–orbit coupling. The *p* orbitals of Sb are projected on the band structure. **c**, **d** Partial charge densities of the valence bands **c** $\Gamma(p_z)$ (isovalue: 0.06 *e* Å^{-3}) and **d** $\Gamma(p_{x,y})$ (isovalue: 0.13 *e* Å^{-3}) at the Γ point in Mg_3Sb_2. **e** The theoretical power factor at 300 K versus Δ of Mg_3Sb_2 at various hole concentrations *p*. The red curve shows the best values corresponding to the optimum carrier concentrations. Data points for unoptimized carrier concentrations fill up the pink area right below the red curve. **f** The experimental power factors[14,15,17–27,39–41] of reported $CaAl_2Si_2$-type compounds at 600 K as a function of Δ. Red points represent the alloys[18,21] with *zT* larger than unity at high temperatures. **a**, **b**, **e**, **f** are adapted with permission from ref. [105], CC-BY-4.0

$_y$ orbitals in the trigonal $CaAl_2Si_2$-type structure. Accordingly, the three-fold degenerate valence band at the Γ point splits into a nondegenerate band $\Gamma(p_z)$ and a doubly degenerate band $\Gamma(p_{x,y})$, where $\Gamma(p_{x,y})$ and $\Gamma(p_z)$ are typically a heavy and light hole band, respectively (Fig. 3a–d).[9,105] The crystal field splitting energy Δ between them is defined as $\Delta = E(\Gamma(p_{x,y})) - E(\Gamma(p_z))$, where the orbital degeneracy is effectively increased when the splitting energy approaches zero. The basic idea of the orbital engineering approach proposed by Zhang et al.[105] is to minimize the splitting energy Δ with the aim to maximize orbital degeneracy and thereby optimize electrical transport performance. This concept is well confirmed by the Boltzmann transport calculations as well as the experimental observations, which show peak values in power factor as $\Delta \approx 0$ (see Fig. 3e, f). As the thermal conductivities of most promising $CaAl_2Si_2$-type TE compounds are comparable especially at high temperatures, the strongly enhanced power factor results in peak *zT* values at $\Delta \approx 0$.[105] The strong correlation between experimental power factors and Δ also indicates the minimal intervalley scattering in different AB_2X_2 compounds, which ensures the success of this approach. Spin–orbit coupling (SOC) is found to lift the degeneracy of the $p_{x,y}$ band, but will not change the main idea of the approach. Accordingly, a simple selection rule, i.e., maintaining the valence band splitting energy around zero (zero-Δ rule), is proposed to optimize the electrical transport performance.

The zero-Δ selection rule may be combined with the band gap criterion $E_g < 1.5$ eV with the aim to search for promising TE candidates from a rich variety of $CaAl_2Si_2(AB_2X_2)$-type compounds. The band gaps of these AB_2X_2 materials show a clear decreasing trend when the electronegativity difference between B and X decreases, which may be rationalized by a decrease of the energy between the atomic orbitals of B and X and an increase in band widths using the molecular orbital scheme.[106,107] However, it should be noted that SOC also plays an important role in decreasing energy gaps of Bi-based compounds.[105] Excellent TE properties are well confirmed in Sb-based and Bi-based compounds such as $EuZn_2Sb_2$,[17] $EuMg_2Bi_2$,[29] and $YbZn_2Sb_2$[15] with small Δ values close to zero and ideal band gaps. In particular, Shuai et al. reported strongly enhanced power factors in $EuMg_2Bi_2$ with a nearly zero Δ value compared with those of $CaMg_2Bi_2$ and $YbMg_2Bi_2$ with Δ values largely deviating from zero,[29] which provides a solid confirmation of the zero-Δ rule. Though simple and powerful, the zero-Δ rule only has resulted in the discovery of a few potential TE candidates.

Materials design and optimization requires effective approaches for manipulating crystal field orbital splitting energy. The hybridizations or overlap integrals of *p* orbitals control their splitting energy at the VBM. In general, tuning structural parameters (for instance, the interlayer distance, bond lengths and angles, and *c*/*a*) by the crystal deformation is able to

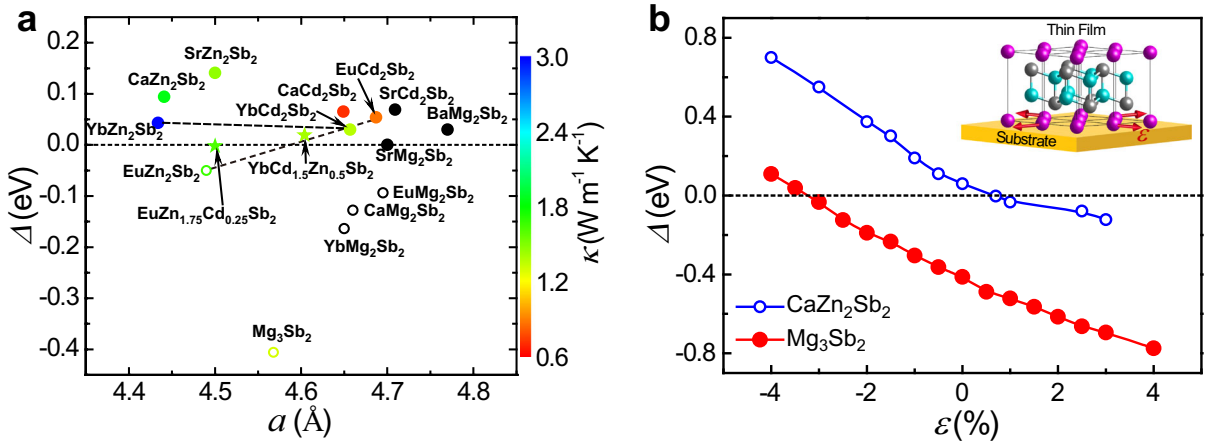

Fig. 4 Solid solution map and biaxial strain engineering for materials design. **a** Calculated Δ versus the lattice constant a in $CaAl_2Si_2$-type compounds with $E_g < 1.5$ eV. Reported thermal conductivities[14,15,17–27,39–41] at 500 K are shown in color bar. The stars correspond to solid solutions $YbCd_{1.5}Zn_{0.5}Sb_2$ and $EuZn_{1.75}Cd_{0.25}Sb_2$ with nearly zero Δ values. **b** Δ as a function of biaxial strain ε in two representative $CaAl_2Si_2$-type compounds Mg_3Sb_2 and $CaZn_2Sb_2$. Biaxial strain ε is defined as $(a - a_0)/a_0 \times 100\%$, where a_0 and a are the in-plane lattice parameters with unstrained and strained states, respectively. Figure is adapted from ref. [105], CC-BY-4.0

effectively manipulate the orbital interactions and thereby the orbital splitting energy. In principle, crystal deformation can be induced by both external and internal forces. External forces include physical pressure and strain effect, while internal forces involve chemical doping or forming solid solutions.[105] Two efficient approaches, solid solution map and biaxial strain engineering, can be used to realize the manipulation of Δ.[105] Using the solid solution map with calculated Δ values versus lattice parameter or band gap E_g, one can conveniently choose two or more compounds with positive and negative Δ values to form a solid solution with the desirable Δ value of zero, which leads to excellent electronic transport performance (see Fig. 4a). Since alloying is also conducive to reducing the thermal conductivity owing to the point defect scattering, strongly enhanced zT values can generally be achieved using this approach. This powerful strategy is confirmed in several alloys including $YbCd_{1.6}Zn_{0.4}Sb_2$,[18] $EuZn_{1.8}Cd_{0.2}Sb_2$,[21] $Eu_{0.2}Yb_{0.2}Ca_{0.6}Mg_2Bi_2$,[29] $YbCd_{1.5}Zn_{0.5}Sb_2$,[35] and $Ca_{0.99}Na_{0.01}MgZnSb_2$[36] with superior TE power factors and zTs. In particular, Wood et al. revealed the valence band crossing in $CaMg_2Sb_2$-$CaZn_2Sb_2$ alloys, which combines with reducing thermal conductivities by the alloy scattering to result in a peak zT of 0.87 at 850 K.[36] As shown by Wang et al., optimizing electrical transport performance induced by minimizing the p orbital splitting energy as well as minimizing the lattice thermal conductivity by the point defect scattering leads to an optimal zT of ~1.3 at 700 K in the $YbCd_{2-x}Zn_xSb_2$ alloys.[35] In addition to the approach of forming solid solutions, biaxial strain engineering can be applied to continuously tune Δ so as to optimize electrical transport performance in thin-film TE materials (see Fig. 4b). A general principle for optimizing TE performance via biaxial strain is that for compounds with negative (positive) Δ value the compressive (tensile) biaxial strain is more effective.

Since most semiconductors show p-orbital characteristics at the valence band edges, the orbital engineering approach can easily be extended to other structures with the same orbital splitting features. One notable extension is the earlier reported pseudo-cubic approach in chalcopyrite structures,[9] where the crystal field splitting energy can be directly linked to the structural deformation parameter $\eta = c/2a$. Moreover, the approach can be extended to layered metal dichalcogenides and lithium intercalated metal dichalcogenides.[105] Therefore, the orbital engineering approach with physical and chemical insights based on the underlying atomic orbitals enriches band engineering and may substantially accelerate the screening and design of new TE materials from layered or noncubic compounds.

MULTI-VALLEY CONDUCTION BANDS, COMPLEX FERMI SURFACE, AND EXCEPTIONAL N-TYPE ELECTRONIC TRANSPORT

The valley degeneracy is defined as the number of different carrier pockets (for the same type of carriers) existing at a given energy level. In general, the valley degeneracy of an individual electronic band can be defined as $N_v = N_{v,sym}N_{v,band}$, where $N_{v,sym}$ is the number of symmetry equivalent positions in the Brillouin zone for a given k point at which the electronic band occurs and $N_{v,band}$ represents the number of electronic bands degenerate at the same k point and energy level. For the high-symmetry Γ point located at the center of the Brillouin zone, $N_{v,sym} = 1$. The orbital engineering approach[105] discussed in the previous section is such a case. Although the band degeneracy $N_{v,band}$ of 3 at the Γ point (at the VBM) can be achieved via tuning the splitting energy of p orbitals, $N_{v,sym}$ of 1 at the Γ point limits the overall valley degeneracy to be $N_v \le 3$. It is thereby clear that a high valley degeneracy requires not only a high band degeneracy $N_{v,band}$ but also a high $N_{v,sym}$. In order to obtain a high $N_{v,sym}$ value, we need a high-symmetry Brillouin zone as well as a band extremum that occurs at a low-symmetry k point.[1,2] Below we will introduce the multi-valley band behavior as the electronic origin of the extraordinary electrical transport performance in n-type Mg_3Sb_2-based TE materials, which exhibit a unique near-edge conduction band minimum (CBM) at a low-symmetry k point with a high $N_{v,sym}$ of 6.

The electronic structure of Mg_3Sb_2 has been studied using different theoretical methods in various reports. Traditional functionals such as GGA[108] or LDA[109] are known to underestimate band gaps while recent calculations[54,74] with the TB-mBJ potential[110] gives more accurate band gaps close to the experimental values. However, band structures in all earlier reports are typically calculated along the high-symmetry k paths,[74–77] which often overlook the actual CBM at the low-symmetry k point. As revealed in the recent calculations including SOC by Zhang et al.,[57] the accurate CBM in Mg_3Sb_2 is located at the CB_1 point (0, 0.417, 0.333), which is along the M^*–L^* line inside the first Brillouin zone (see Fig. 5a). Mg_3Sb_2 shows an indirect band gap of ~0.6 eV with the VBM at the Γ point and the CBM at the CB_1 point. Moreover, there is a secondary band minimum

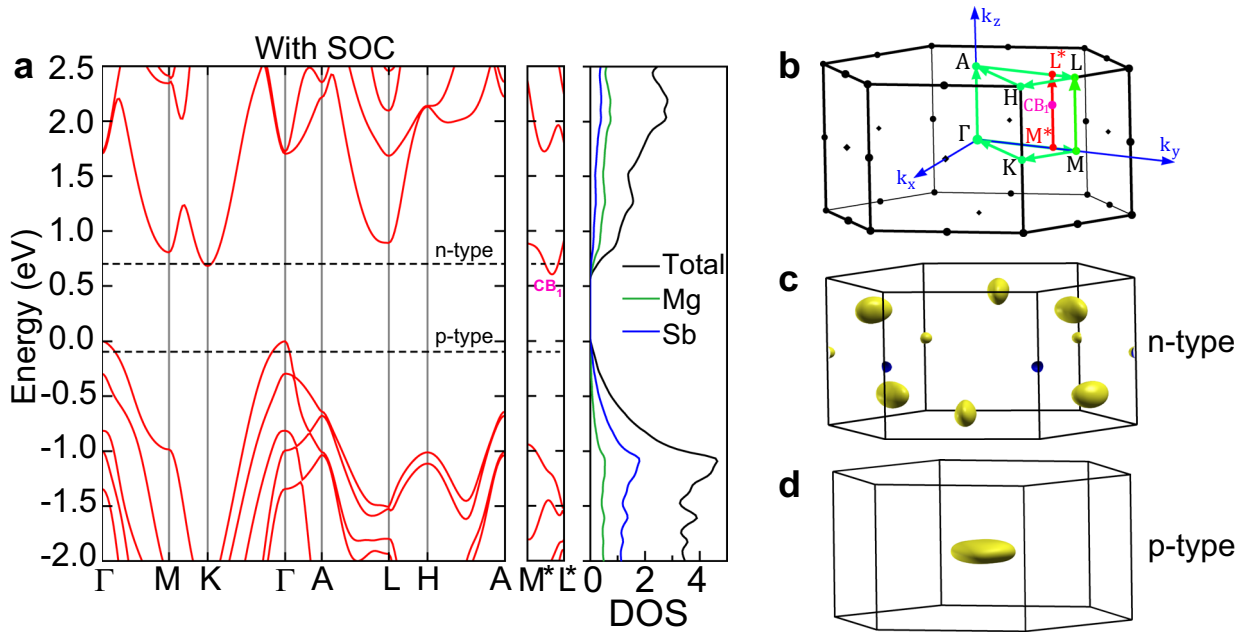

Fig. 5 **a** Band structure and partial density of states of Mg_3Sb_2 by TB-mBJ potential with SOC. **b** High-symmetry *k* points and *k* paths in the Brillouin zone. **c** Multiple carrier pockets shown in Fermi surface of n-type Mg_3Sb_2 for an energy level at 0.1 eV above the conduction band minimum CB_1. **d** One highly anisotropic carrier pocket at the Γ point shown in Fermi surface of p-type Mg_3Sb_2 corresponding to an energy level at 0.1 eV below the valence band maximum. **a**, **b** are adapted with permission from ref. [57], American Chemical Society. **c**, **d** are adapted with permission from ref. [54], CC-BY-4.0

located just above the CB_1 extremum at the K point. The small energy difference ΔE_{K-CB_1} of 0.078 eV between the two band minima CB_1 and K suggests that they might even be treated as effectively converged at elevated temperatures because of the thermal broadening of Fermi function. Inspired by the biaxial strain engineering[105] in p-type compounds, Li et al. revealed that n-type electrical performance of Mg_3Sb_2 can also be optimized by tuning ΔE_{K-CB_1} towards zero via the biaxial strain.[111]

The iso-energy Fermi surface provides an intuitive shortcut to understand the multi-valley conduction bands in Mg_3Sb_2 (see Fig. 5b–d). In contrast to only one highly anisotropic hole pocket of the VBM at the Γ point, the Fermi surface of n-type Mg_3Sb_2, corresponding to an energy level 0.1 eV above the conduction band minimum CB_1, shows 6 isolated full electron pockets inside the Brillouin zone and 6 one-third pockets at the K point (see Fig. 5c).[54] As a result, the valley degeneracies for the conduction band minima CB_1 and K are, respectively, 6 and 2, which may be added up to 8 when they are effectively converged. Such a high valley degeneracy is comparable to many state-of-the-art TE materials such as $(Bi,Sb)_2Te_3$ and PbTe.[2,103]

The complex Fermi surface is conducive to good TE performance. As proposed by Gibbs et al.,[112] the complexity of Fermi surface may be characterized by the simplified parameter $N_v^* K^*$, where N_v^* and K^* represent the effective valley degeneracy and anisotropy parameter of a single carrier pocket, respectively. In general, the higher the $N_v^* K^*$, the better the electrical transport performance. In addition to the high valley degeneracy, the complexity of Fermi surface in n-type Mg_3Sb_2 is clearly reflected in the ellipsoidal-like carrier pockets at the CB_1, indicating a clear anisotropic feature. For every individual carrier pocket at the CB_1 point, the effective mass is anisotropic along one longitudinal (elongated) and two transverse directions in *k* space with $m_{\|}^* = 0.55m_e$, $m_{\perp,1}^* = 0.21m_e$, and $m_{\perp,2}^* = 0.28m_e$, although when averaging over the six equivalent carrier pockets the overall average effective mass tensor follows the crystal symmetry and shows a nearly isotropic feature with $m_{kx}^* = m_{ky}^* = (0.21 \times 4 + 0.55 \times 2)/6 = 0.32m_e$ and $m_{kz}^* = 0.28m_e$.[113] Regarding the Fermi surface complexity, it is crucial to take into account the contribution of the anisotropic feature of the single carrier pocket at the CB_1, which shows a moderate anisotropy parameter $K = m_{\|}^*/(m_{\perp,1}^* m_{\perp,2}^*)^{1/2} \approx 2.3$.

The Fermi surface complexity factor $N_v^* K^*$ can be calculated by $(m_d^*/m_c^*)^{3/2}$,[112,114] where m_c^* is evaluated using the carrier density *n* and theoretical electrical conductivity σ/τ from a BoltzTraP[115] calculation by $m_c^* = ne^2/(\sigma/\tau)$ under the constant carrier's scattering time approximation.[116] m_d^* is estimated by fitting the Seebeck coefficient from Boltzmann transport calculations applied to the full DFT band structure using the single band model. The theoretical calculations reveal a peak $N_v^* K^*$ of ~19 in n-type Mg_3Sb_2, much higher than that of p-type Mg_3Sb_2 (see Fig. 6a).[113] This is consistent with both the theoretical and experimental results (see Fig. 6b, c), displaying significantly enhanced power factors for n-type doping in comparison with those for p-type doping in Mg_3Sb_2-based materials. The high Fermi surface complexity, as well as the superior n-type electrical transport performance, can be attributed to a combined effect of the large m_d^* induced by the high valley degeneracy, the light conductivity effective mass, and the carrier pocket anisotropy (see Fig. 6a). The n-type transport of Mg_3Sb_2 shows a primary contribution from the nontrivial band minimum CB_1 as well as a certain contribution from the secondary band minimum at the K point. This multiple band behavior in n-type Mg_3Sb_2 is confirmed by the result from the BoltzTraP calculation that Mg_3SbBi with a much larger ΔE_{K-CB_1} of ~0.18 eV shows lower Seebeck coefficients in comparison with those of Mg_3Sb_2 (see Fig. 6d).

Though the multiple conduction band behavior was also found in ternary AMg_2X_2 and AZn_2Sb_2,[117] the unique conduction band CB_1 with a six-fold valley degeneracy only exists in binary Mg_3X_2 (X = As, Sb, and Bi). As shown by the theoretical calculations of Sun et al., the unique CBM at the CB_1 point in Mg_3Sb_2 might possibly be explained by the bonding states between Mg1 and Mg2 atoms.[118] However, the very large interatomic distance between Mg1 and Mg2 (~3.7 Å) indicates that the orbital interaction between Mg1 and Mg2, if any, should be very weak.

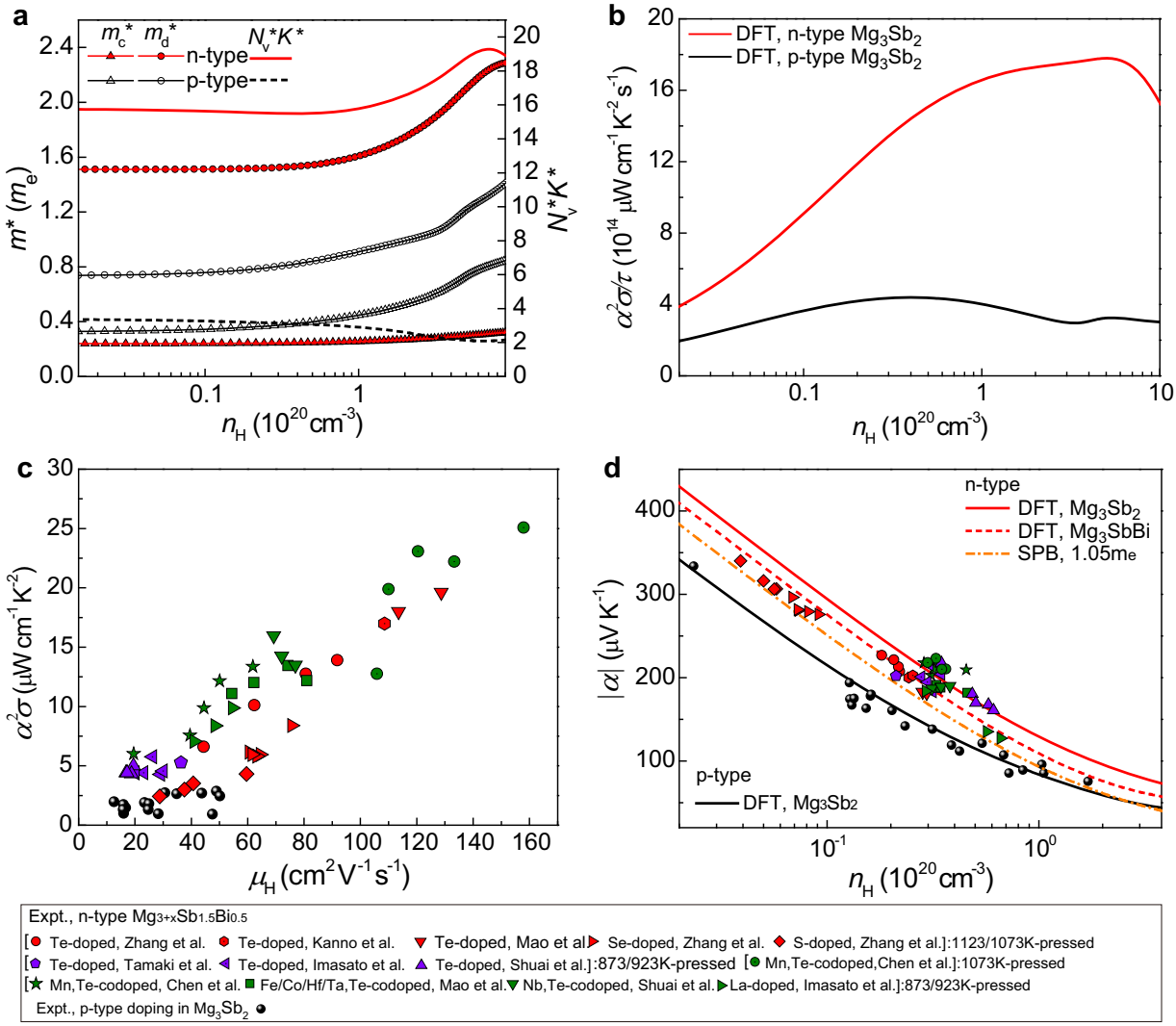

Fig. 6 **a** Conductivity effective mass m_c*, density of states (DOS) effective mass m_d*, and Fermi surface complexity factor N_v*K* estimated from BoltzTraP[115] as a function of Hall carrier concentration (n_H) in p-type and n-type Mg_3Sb_2.[113] n_H is estimated by $1/eR_H$, where R_H is Hall coefficient. **b** Theoretical power factor[54] at 300 K from BoltzTraP versus n_H in Mg_3Sb_2. **c** Experimental power factor versus Hall mobility at room temperature for reported p-type and n-type Mg_3Sb_2-based materials. **d** Seebeck coefficient values ($|\alpha|$) as a function of n_H at 300 K. The black and red solid lines correspond to the prediction of p-type and n-type Mg_3Sb_2 from BoltzTraP, taken from ref. [54]. The orange dash-dotted line shows the prediction by a single parabolic band (SPB) model with a DOS effective mass equal to that of the CB_1 band at the CBM of Mg_3Sb_2.[54] The red dashed line represents the theoretical prediction of n-type Mg_3SbBi taken from ref. [113]. In **c**, **d**, experimental data of p-doped Mg_3Sb_2 and n-doped $Mg_{3+x}Sb_{1.5}Bi_{0.5}$ are taken from refs. [41,45–47,49,50] and refs. [54–60,63,64,66,67,71], respectively

Moreover, the calculations were only conducted for Mg_3Sb_2 without a systematic comparison with many other ternary compounds. The underlying origin of the unique six-fold CB_1 band minimum in Mg_3X_2 still requires further investigation. In Mg_3X_2, the band gaps decrease from Mg_3As_2 (1.6 eV) to Mg_3Sb_2 (0.6 eV) to Mg_3Bi_2 (semimetal). It is found that doping or substituting on the anion sites will not destroy the favorable conduction band minimum CB_1 since the conduction bands are mainly contributed by the electronic states of Mg (Fig. 5a).[54,57] Therefore, n-doped Mg_3Sb_2, Mg_3As_2, as well as the solid solutions $Mg_3Sb_{2-x}Bi_x$, $Mg_3Sb_{2-x}As_x$, and $Mg_3As_{2-x}Bi_x$ with suitable band gaps are predicted to show promising electrical transport performance if they are properly doped on the anion sites.[54]

Experimentally, we are especially interested in n-type $Mg_3Sb_{2-x}Bi_x$ with the energy gaps $E_g \leq \sim 0.6$ eV within $\sim 10k_BT$ ($T = 300$–725 K), which is generally the suitable value for a good TE material.[119] DFT calculations[113] with the TB-mBJ potential reveal the accurate conduction band alignments of $Mg_3Sb_{2-x}Bi_x$ alloys (see Fig. 7a), which makes a correction to the simple schematic plot by Imasato et al.[62] The Mg_3Bi_2 alloying results in a moderate increase in the energy separation between conduction band minima K and CB_1, making the contribution of the secondary band minimum K to electronic transport insignificant. The conduction band minimum Γ ($N_v = 1$) shows a noticeable downward shift with the Mg_3Bi_2 alloying. However, the band minimum Γ is too far from the band minimum CB_1 to play a significant role in n-type electronic transport before the band-gap closure ($x \approx 1.7$). As the composition of Mg_3Bi_2 increases in $Mg_3Sb_{2-x}Bi_x$ solid solutions, the band gap is linearly reduced from ~0.6 eV ($x = 0$) to ~0.24 eV ($x = 1$) to zero (semimetal, $x \approx 1.7$), indicating an increasing detrimental bipolar contribution. In addition, the narrowing of the band gap, accompanied by the increasing near-edge band widths, results in the decreasing band effective masses. This is confirmed in several reports[62,111] as well as the theoretical result[113] by BoltzTraP (Fig. 7b), which shows a clear decreasing trend in m_c^* of near-edge conduction bands from Mg_3Sb_2 to Mg_3SbBi to Mg_3Bi_2.

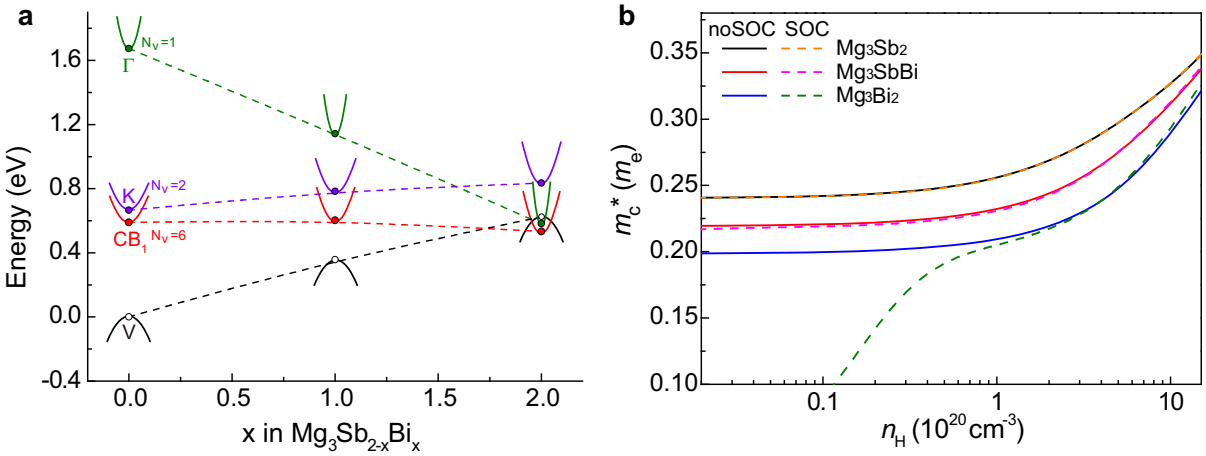

Fig. 7 **a** The conduction band alignments in $Mg_3Sb_{2-x}Bi_x$ ($x = 0$, 1, and 2) solid solutions by the TB-mBJ method with SOC.[113] It should be noted that the three conduction band minima are located at different k points (i.e., CB_1, K, and Γ). The band alignment is calculated by aligning the Mg-1s core levels of different compounds. The valence band maximum of Mg_3Sb_2 at the Γ point is set to 0 eV. **b** Conductivity effective mass versus Hall carrier concentration simulated from BoltzTraP for n-type $Mg_3Sb_{2-x}Bi_x$.[113] SOC and noSOC denote the cases with and without SOC, respectively. It is clear that SOC has a negligible effect on near-edge conduction bands in $Mg_3Sb_{2-x}Bi_x$ because the CBM is dominated by electronic states of the light element Mg (see Fig. 5a). Figure is adapted from ref. [113]

Although the Mg_3Bi_2 alloying lowers the Seebeck coefficient due to the lighter conduction band mass and the weaker contribution from the secondary band minimum *K*, it is conducive to increasing the carrier mobility and weighted mobility as the conductivity effective mass m_c^* is decreased (see Fig. 7). An appropriate amount of the Mg_3Bi_2 alloying ($x \le 1$) would be ideal for n-doped $Mg_3Sb_{2-x}Bi_x$ to have an enhanced weighted mobility for superior TE performance without a noticeable bipolar effect at elevated temperatures. This is consistent with the widely reported compositions of n-doped $Mg_3Sb_{2-x}Bi_x$ ($x = 0$, 0.5, and 1) with excellent high-temperature TE performance. An increasing bipolar effect with increasing Bi content in $Mg_3Sb_{2-x}Bi_x$ is expected to shift the peak *zT* to lower temperatures, but an improved *zT* at low temperatures may be achieved owing to the lighter conductivity effective mass. Thus more efforts should be made to investigate n-type $Mg_3Sb_{2-x}Bi_x$ with a wider range of compositions ($x = 0$–1.7). It will also be interesting to design a functionally graded n-doped $Mg_3Sb_{2-x}Bi_x$ ($x = 0$–1.7) system for TE applications. Below we give a brief overview of the recent experimental reports on n-doped $Mg_3Sb_{2-x}Bi_x$.

As shown originally by Pedersen[53] in 2012 (see the link in ref. [53] for details) and later reported by Tamaki et al.[55] and Zhang et al.[54], an exceptionally high n-type TE performance can be achieved in $Mg_3Sb_{1.5}Bi_{0.5}$ through Te doping on the anion site with or without excess Mg. Zhang et al.[54] reported n-type $Mg_3Sb_{1.5-0.5x}Bi_{0.5-0.5x}Te_x$ with varying Te content and no excess Mg synthesized by combining arc melting and spark plasma sintering (SPS) at 1123 K based on the reproduction and improvement of the original work by Pedersen.[53] The samples with an optimal *zT* of 0.56–1.65 at 300–725 K reported by Zhang et al.[54] show the intrinsic temperature-dependent mobility with the dominant acoustic phonon scattering at low temperatures. Tamaki et al.[55] reported n-type $Mg_{3.2}Sb_{1.5}Bi_{0.49}Te_{0.01}$ with a large nominal excess Mg prepared using ball milling followed by SPS pressing at 873 K, which exhibits low carrier mobility and TE performance below 500 K due to impurity scattering. Later, two approaches were applied to improve the mobility and power factor at low temperatures (Fig. 6c) by tuning the carrier scattering mechanism from the ionized impurity scattering to the acoustic-phonon-dominated mixed scattering. One approach is to dope $Mg_{3.2}Sb_{1.5}Bi_{0.5}$ with the transition metals (i.e., Nb, Fe, Co, Hf, Ta, and Mn) on the Mg sites and the Te dopant on the anion sites using a pressing temperature of 927 K as reported by Shuai et al.,[56] Mao et al.,[58] and Chen et al.[66] Following the earlier work of Zhang et al.,[54] the other approach is to increase the pressing temperature to 1123 or 1073 K, which was also confirmed in the studies by Kanno et al.[64] and Mao et al.[59] Combining the above two approaches, Chen et al.[71] was able to further improve the room-temperature *zT* and average *zT* in n-type porosity-mediated $Mg_{3.225}Mn_{0.025}Sb_{1.5}Bi_{0.49}Te_{0.01}$ with an SPS pressing temperature of 1073 K. Regarding the underlying mechanism, Mao et al.[59] suggested that the increasing mobility might be due to reduction of the number of Mg vacancies, whereas Kuo et al.[120] proposed an illuminating two-phase model that explains the experimental observation by the larger grain sizes reducing the grain boundary electrical resistance under a higher pressing temperature. In addition, enhanced low-temperature TE performance was shown in n-type $Mg_{3.2}SbBi_{0.99}Te_{0.01}$ and Te-doped $Mg_3Sb_{0.6}Bi_{1.4}$ by Imasato et al.[62,70] and $Mg_{3.02}Sb_yBi_{1.99-y}Te_{0.01}$ ($y = 1.1$–1.5) by Shu et al.[68] with increasing Bi content, which can be attributed to the lighter conductivity effective mass. Regarding n-type dopants other than the Te element, Se[57] and S[60] on the anion site as well as La[67] and Y[69] on the cation site have also been experimentally explored in $Mg_{3+x}Sb_{1.5}Bi_{0.5}$. With continuous experimental efforts, a low-temperature *zT* of ~0.9 at 323 K and a peak *zT* of ~1.85 at 723 K have been achieved so far in n-type (Mn, Te)-codoped $Mg_3Sb_{1.5}Bi_{0.5}$.[66,71] In addition to the intensive developments in TE performance, the thermal stability of n-type Te-doped $Mg_3Sb_{1.5}Bi_{0.5}$ was investigated by Jørgensen et al.[72] using synchrotron powder X-ray diffraction and X-ray total scattering, where a clear evolution of bismuth as a secondary phase was observed in the powdered sample during thermal cycling.

Several experimental and theoretical efforts[54,60,61,63,65,121,122] reveal that a large amount of excess Mg is not needed for achieving n-type properties as claimed by Tamaki et al.[55]. A tiny amount of excess Mg or even no excess Mg is required to realize n-type properties as long as great care is taken to avoid the Mg loss during the synthesis, consistent with the earlier report without excess Mg by Zhang et al.[54] The samples with smaller amounts of excess or no excess Mg even show better performance and stability than those with large amounts of excess Mg.[63,122] Various reports with different amounts of excess Mg may arise from the difficulty in preparing these materials without the Mg loss due to the high reactivity, easy oxidation, and high vapor pressure of Mg.

DEFECT-CONTROLLED CARRIER TRANSPORT, ELECTRONEGATIVITY, AND BONDING CHARACTER

Nearly all $CaAl_2Si_2$-type compounds, except $CaAl_2Si_2$[123] and $SrAl_2Si_2$[124], have been reported as intrinsically p-type, which is attributed to the intrinsic point defects pinning the chemical potential close to the valence bands. According to the intrinsic defect calculations,[80,125] the cation vacancy at the A site is the most energetically stable point defect in all AZn_2Sb_2 (A = Ca, Sr, Eu, and Yb) compounds, which leads to the persistent p-type behavior in these compounds. Pure Mg_3Sb_2 is intrinsically p-type, and many attempts at doping or substituting with a series of elements result in p-type behaviors as well.[38–50,52,102,126–130] This is because of the low formation energies of the negatively charged Mg vacancies (V^{2-}_{Mg1} and V^{2-}_{Mg2}) (Fig. 8), which prevent the chemical potential from moving close to the conduction bands for the Sb-rich condition.[55,61] The n-type doping in Mg_3Sb_2-based materials is challenging and only recently discovered to be successful.[51,53–55] Several defect calculations[55,61,121] were conducted to explain the n-type behavior in Mg_3Sb_2 under the Mg-excess condition. The results vary from different methods applied in defect energy calculations. Ohno et al.[61] concluded from calculations using the PBE functional[108] with finite-size and band-gap corrections that under the Mg-excess condition the Mg vacancy suppression rather than the Mg interstitial[55] is responsible for n-type properties (Fig. 8), while Chong et al.[121] based on more accurate calculations with the HSE06 functional[131] revealed that the role of the excess Mg for achieving n-type behavior is to compensate the electronic charge of the defect complex $(V_{Mg2} + Mg_i)^{1-}$. It is clear that defect calculations are usually sensitive to the applied theoretical methods; however, the robust relative trend of defect formation energies is supposed to render insightful guidance for the carrier transport. Below we introduce guidelines for the defect-controlled carrier transport with respect to the electronegativity in p-type AZn_2Sb_2- and n-type Mg_3Sb_2-based materials.

In p-type AZn_2Sb_2 (A = Ca, Sr, Eu, and Yb), the experimental carrier density increases with increasing electronegativity[132] of A (Fig. 9a). As revealed by Pomrehn et al.[80] using DFT calculations, the increasing carrier density can be rationalized by the decreasing trend in the vacancy formation energy at the cation A site with increasing electronegativity (Fig. 9b). The relationship between the vacancy defect-formation energy and electronegativity might be related to the relative energy cost of the electron transfer influenced by the bond strength between the cation A and the anion, which in turn affects the vacancy formation energies. In general, the formation of the vacancy is easier when the bonding is weak. However, in order to explain the deduction, accurate calculations should be conducted to characterize the bond strength between A and Sb. Though the underlying mechanism regarding the bond strength is complicated, the results provide insight on tuning carrier density by alloying on the A site with elements of varying electronegativities. This idea is well confirmed in many significant reports[15,19,23,32] on optimizing p-type AB_2X_2 TEs, where excellent zTs were achieved owing to the carrier density optimization and thermal conductivity reduction via alloying at the A site.

Defect-controlled carrier transport with the insight from the electronegativity[133] difference was explored in n-type $Mg_3Sb_{1.5}Bi_{0.5}$ with the chalcogens Q (S, Se, and Te) as electron dopants.[60] Experimentally, it is found that both the maximum attainable carrier concentration and mobility increase with decreasing electronegativity difference $|\chi_Q - \chi_{Mg}|$ between the chalcogen dopants Q and Mg (Fig. 9c). Using DFT calculations, Zhang et al.[60] revealed that the improving carrier concentration is caused by the increasing doping limit induced by the lower extrinsic defect-formation energy (Fig. 9d), which may be explained by the stronger bonding between the dopant and the matrix with decreasing $|\chi_Q - \chi_{Mg}|$. Moreover, the enhanced mobility is attributed to the smaller effective mass of conduction bands originating from the enhanced bond covalency with decreasing electronegativity difference,[134,135] which is supported by the decreasing theoretical density of states. According to the above trends, using dopants with a small electronegativity difference compared to its bonding partner was proposed as a guiding rule for efficient n-type doping in Mg_3Sb_2-based compounds.[60] As confirmed in extrinsic defect calculations for n-type Mg_3Sb_2 by Gorai et al.,[136] this guideline was found to work pretty well for the anion site doping but might not work well for the cation site doping due to the strong charge compensation and complex competing phases involved. Moreover, theoretical calculations by Gorai et al.[136,137] suggested the group-3 elements including La, Y, and Sc as effective n-type cation dopants for Mg_3Sb_2, which was confirmed by the recent experiments[67,69] of La-doped and Y-doped $Mg_{3+x}Sb_{1.5}Bi_{0.5}$.

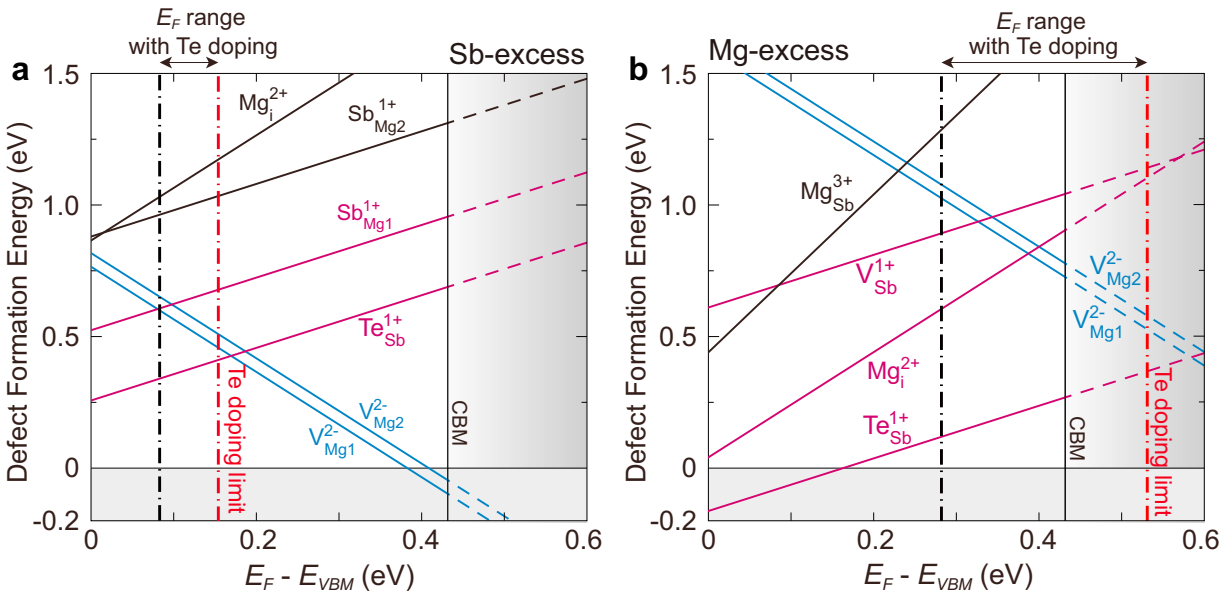

Fig. 8 **a**, **b** Defect formation energies of intrinsic point defects as well as the extrinsic defect Te_{Sb} under **a** Sb-excess ($\Delta\mu_{Sb} = 0$) and **b** Mg-excess ($\Delta\mu_{Mg} = 0$) conditions. Figure is adapted with permission from ref. [61], Elsevier

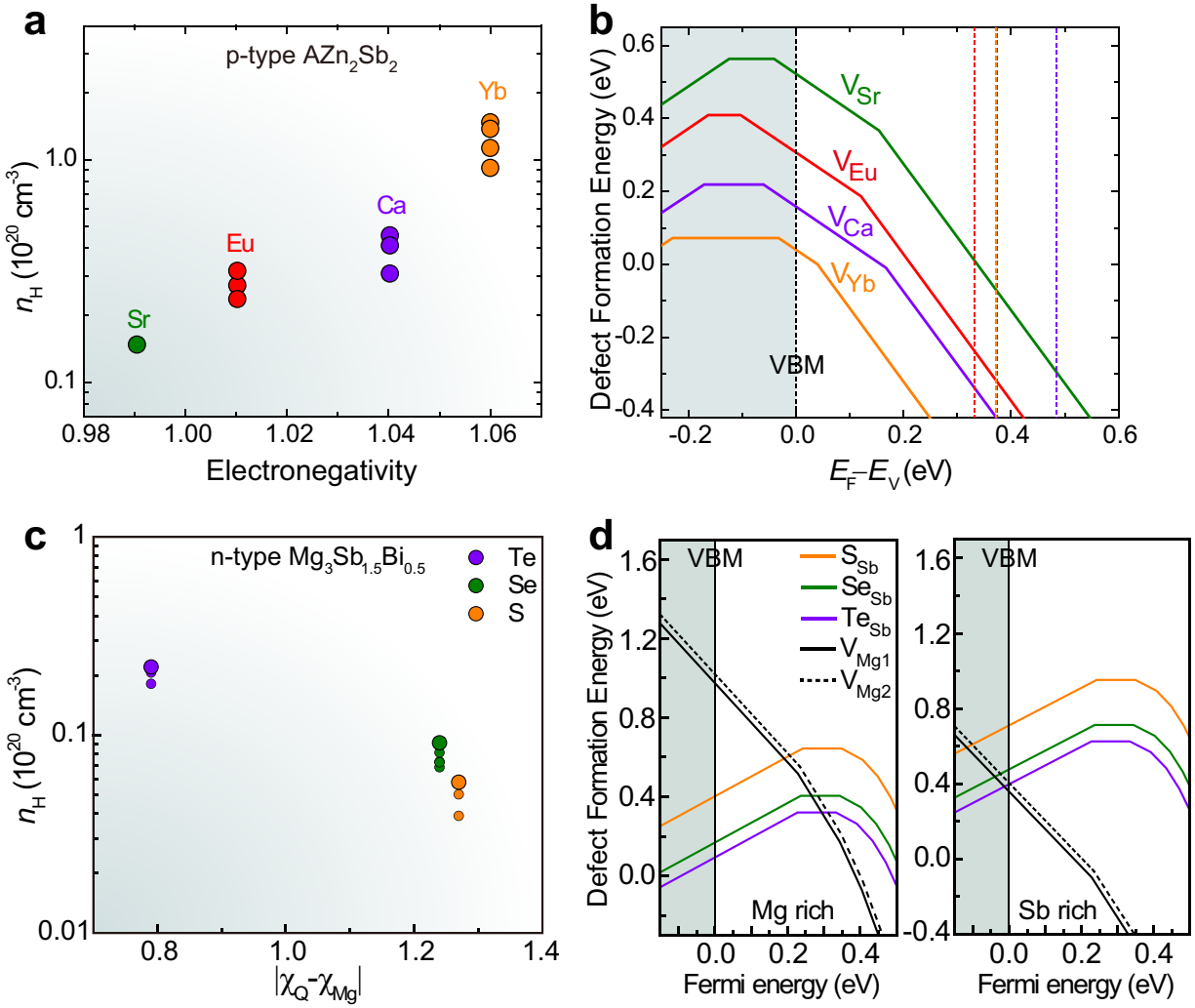

Fig. 9 Defect-controlled carrier density. **a** The experimental Hall carrier concentration[15–17,20,95] at room temperature versus the electronegativity of the cation A (A = Sr, Eu, Ca, and Yb) in p-type AZn_2Sb_2. The Allred–Rochow scale[132] of the electronegativity is used. **b** Defect formation energy of the cation vacancy in AZn_2Sb_2. The respective conduction band minima of different compounds are shown in the colored dashed lines. **c** Hall carrier concentration[54,57,60] at 300 K as a function of the electronegativity difference $|\chi_Q - \chi_{Mg}|$ (Q = S, Se, and Te) in n-type chalcogen-doped $Mg_3Sb_{1.5}Bi_{0.5}$. The Pauling scale[133] of the electronegativity is adopted. **d** Defect formation energies of extrinsic defects Q_{Sb} as well as the intrinsic defects V_{Mg1} and V_{Mg2} under Mg-rich and Sb-rich conditions. **a**, **b** and **c**, **d** are adapted with permissions, respectively, from refs. [80] and [60], Wiley-VCH

ANHARMONIC PHONON MODES AND LOW LATTICE THERMAL CONDUCTIVITY

Reported lattice thermal conductivities[14–69,71] κ_L at room temperature in $CaAl_2Si_2$-type TE compounds span a relatively wide range from ~0.6 $W\,m^{-1}\,K^{-1}$ in $CaCd_2Sb_2$ to ~4.5 $W\,m^{-1}\,K^{-1}$ in $CaMg_2Sb_2$. Among them, Mg_3Sb_2 with a low density of ~4.0 g cm^{-3} shows an intrinsically low room-temperature κ_L of about 1.0–1.5 $W\,m^{-1}\,K^{-1}$,[40,45,46] comparable to those of the state-of-the-art TE materials PbTe and Bi_2Te_3.[1,138,139] A small difference (~15%) in κ_L is found between single crystalline and polycrystalline Mg_3Sb_2 samples,[40,102,130] suggesting that the grain boundary scattering[83] does not play a significant role in phonon transport. Though alloying is often applied to further reducing lattice thermal conductivity through point defect scattering, the intrinsically low thermal conductivity induced by the phonon–phonon scattering is indispensable to the exceptionally high *zT* in n-type Mg_3Sb_2-based materials. Below we will discuss the origin of the intrinsically low lattice thermal conductivity in Mg_3Sb_2 from first principles.

The lattice thermal conductivity of Mg_3Sb_2 and the two ternary analogs ($CaMg_2Sb_2$ and $CaMg_2Bi_2$) was calculated by Zhang et al.[84] using first-principles Boltzmann transport calculations considering the anharmonic phonon–phonon scattering with the ShengBTE[140] code. Importantly, the theoretical result shows a noticeable decrease in κ_L from $CaMg_2Sb_2$ and $CaMg_2Bi_2$ to Mg_3Sb_2, which is in good agreement with experiments (see Fig. 10a). It is found that the phonon lifetime plays a key role in reducing κ_L in Mg_3Sb_2.[82,84] In general, the phonon lifetime for intrinsic crystalline materials is dominated by the three-phonon anharmonic scattering process. As revealed in Fig. 10b, the calculated anharmonic scattering rates of Mg_3Sb_2 are considerably larger than those of $CaMg_2Sb_2$ and $CaMg_2Bi_2$ in the low- and mid-frequency regions (<5.5 THz). In particular, the anharmonic scattering rates of Mg_3Sb_2 display one peak at 0.7–1.04 THz and two peaks in the mid-frequency region of 3.3–4.8 THz, which are about (or even more than) one order of magnitude larger than those of ternary compounds within the same frequency regions. The peak in anharmonic scattering rates of Mg_3Sb_2 at 0.7–1.04 THz is typically induced by a unique feature in phonon dispersion in

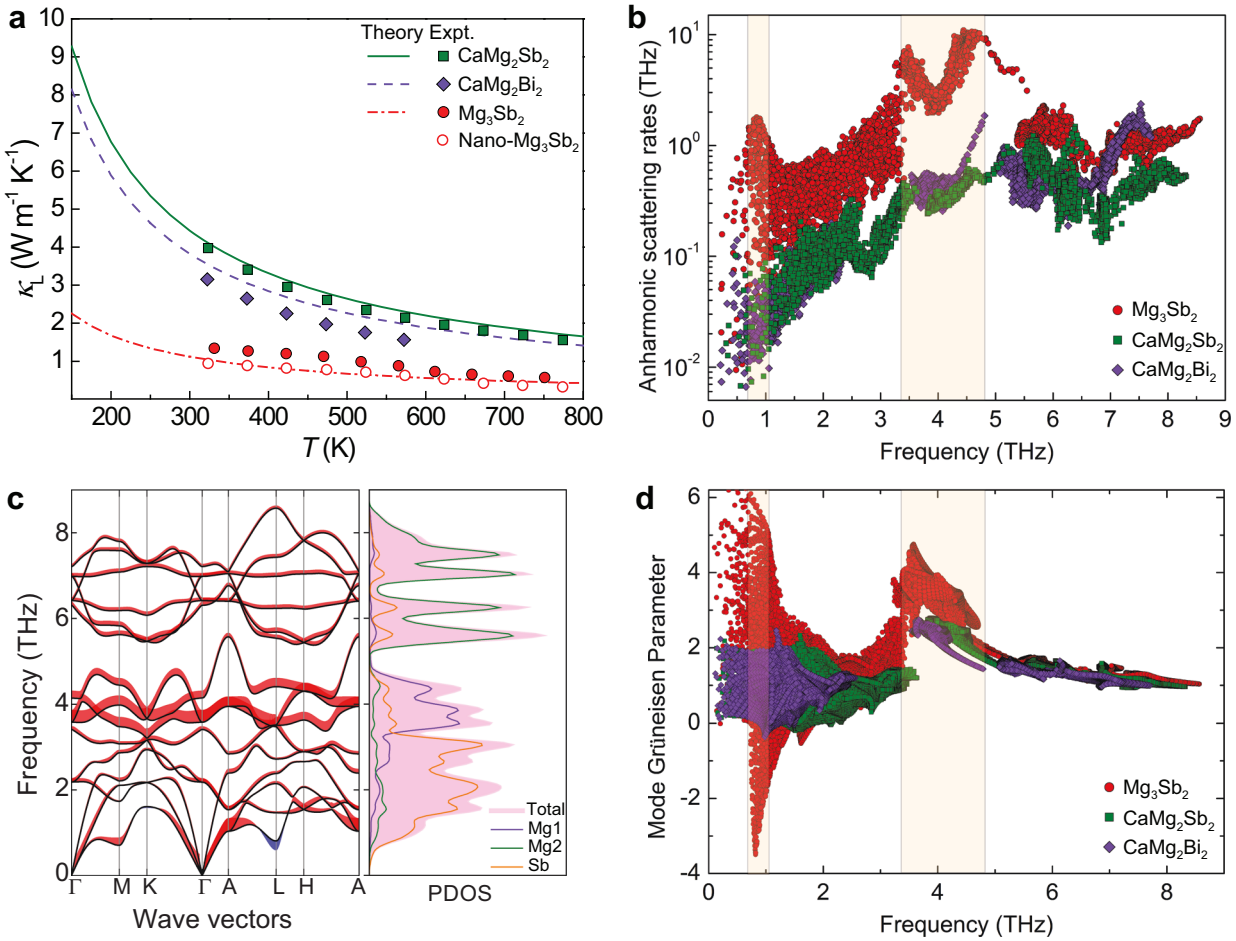

Fig. 10 **a** The experimental and theoretical lattice thermal conductivities. The theoretical and experimental data are taken from refs. [79,84] and [26,36,40,43], respectively. Nano-Mg_3Sb_2 denotes the nanostructured Mg_3Sb_2 sample[43] prepared by the high-energy ball milling method. **b** The calculated anharmonic scattering rates of Mg_3Sb_2, $CaMg_2Sb_2$, and $CaMg_2Bi_2$.[84] **c** Phonon band structure and density of states of Mg_3Sb_2. Adapted with permission from ref. [79], CC-BY-4.0. The mode Grüneisen parameters are projected on the phonon band structure.[84] Curve width indicates the relative magnitude of the mode Grüneisen parameter. The positive and negative mode Grüneisen parameters are colored in red and blue, respectively. **d** Mode Grüneisen parameters of Mg_3Sb_2, $CaMg_2Sb_2$, and $CaMg_2Bi_2$.[84] For the theoretical results shown here, the longitudinal optical/transverse optical (LO/TO) splitting is not considered since the LO/TO splitting only has a minor effect on the results.[84] The readers are referred to ref. [82] for the results considering the LO/TO splitting

comparison with ternary compounds as pointed out earlier by Peng et al.,[82] i.e., much softer transverse acoustic phonon modes at the M (~0.71 THz), L (~0.81 THz), and A (~1.04 THz) points characterized by very large mode Grüneisen parameters (Fig. 10c, d). In particular, the soft transverse acoustic phonon mode at the L point exhibits the largest negative mode Grüneisen parameter. A similar behavior was also found in Mg_3Bi_2, where the phonon calculations often show negative (imaginary) frequencies for transverse acoustic branches at the L point. In addition, the peak anharmonic scattering rates of Mg_3Sb_2 at 3.3–4.8 THz in Mg_3Sb_2 are induced by the anharmonic optical phonon modes within this frequency region with much larger mode Grüneisen parameters than those of $CaMg_2Sb_2$ and $CaMg_2Bi_2$ (Fig. 10d). Therefore, the soft transverse acoustic phonon modes within 0.7–1.04 THz as well as the anharmonic optical modes within 3.3–4.8 THz contribute to the large peak values in the anharmonic scattering rates and thereby intrinsically low lattice thermal conductivity in Mg_3Sb_2.

The unique soft transverse phonon modes are related to the structural instability in Mg_3Sb_2 and Mg_3Bi_2, which is well confirmed in their less negative formation enthalpies[141,142] compared with other $CaAl_2Si_2$-type compounds (Fig. 11a). As claimed by Peng et al.,[82] the soft transverse acoustic phonon modes in Mg_3Sb_2 and Mg_3Bi_2 may be attributed to the unstable Mg1 in the octahedral sites as judged by the small cation-to-anion ionic radius ratio below the stability limit (0.414), which results from the small ionic radius of Mg (Fig. 11b). Although the insight proposed by Peng et al.[82] is illuminating, it cannot explain why Mg_3As_2, which also exhibits a cation-to-anion ionic radius ratio below the stability limit, does not show soft transverse acoustic phonon modes. Clearly, the ionic radius ratio rule is somewhat oversimplified by assuming purely ionic bonding with a complete charge transfer. In reality, chemical bonds in Mg_3X_2 show certain degrees of covalency with incomplete charge transfers (see Table 1), which will result in a larger effective ionic radius of Mg1 and probably push the cation-to-anion ionic radius ratio above the stability limit.

The instability of Mg1 is well confirmed in the relatively larger atomic displacement parameter and flatter potential energy landscape of Mg1 compared to those of Mg2 in Mg_3Sb_2 (Fig. 11c, d),[79] which might be attributed to the relatively weaker Mg1-Sb bond as well as the larger void space of the octahedral site of Mg1. However, the unstable Mg1 at the octahedral site better explains the anharmonic optical modes at 3.3–4.8 THz rather than the soft transverse acoustic modes since the anharmonic optical modes

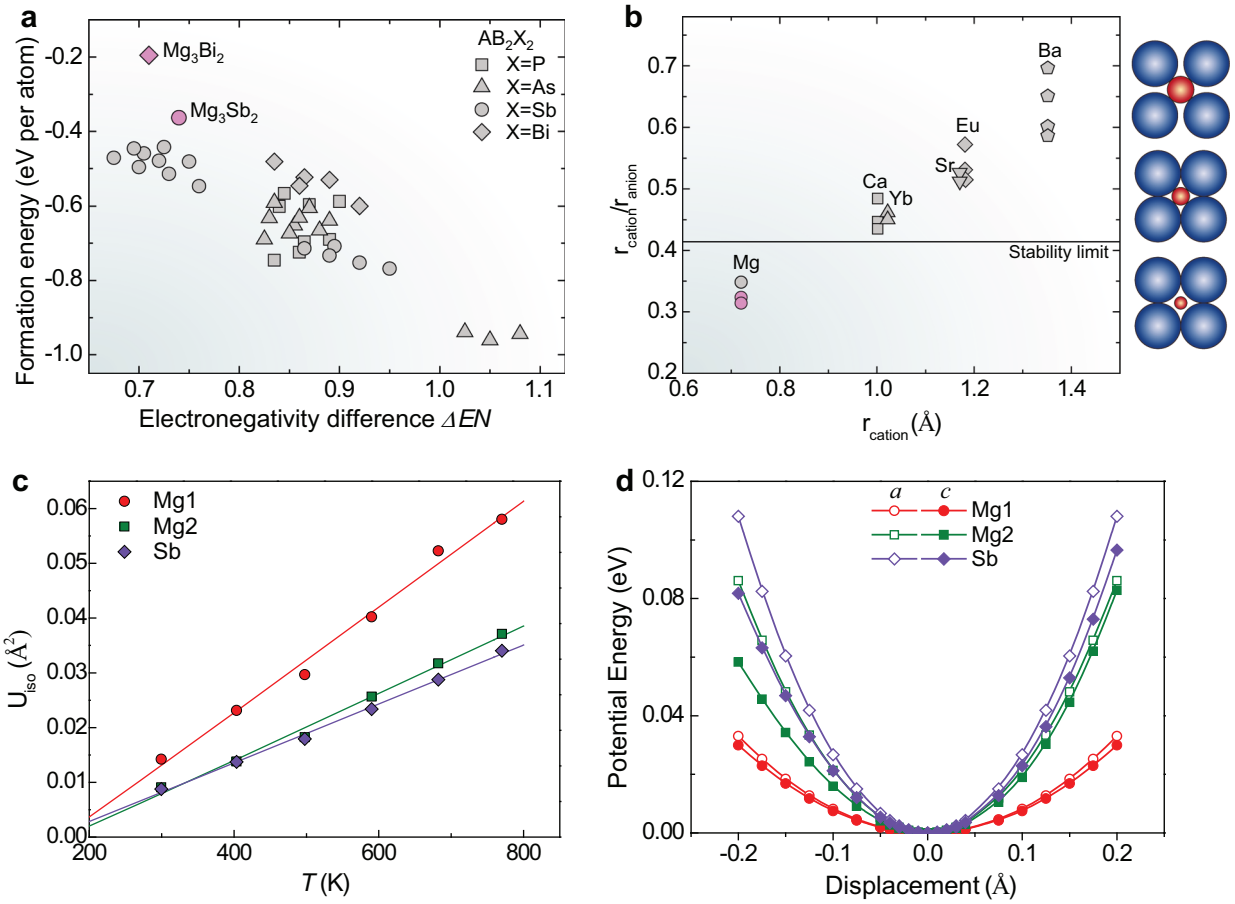

Fig. 11 **a** Formation enthalpy versus the electronegativity difference ΔEN in AB_2X_2 ($CaAl_2Si_2$-type) compounds. ΔEN is calculated by the difference between the electronegativity of the anion X and the average electronegativity of the atoms A and B. Formation enthalpy values are taken from MaterialsProject.org.[141,142] **b** The cation-to-anion ionic radius ratio r_{cation}/r_{anion} versus the ionic radius of the cation A at the octahedral site in AMg_2X_2. The minimum stability limit of r_{cation}/r_{anion} for the octahedral site is 0.414. The data points for Mg_3Sb_2 and Mg_3Bi_2 are colored in pink. Adapted with permissions from ref. [82], Elsevier. **c** Experimental isotropic atomic displacement parameters of Mg_3Sb_2. **d** The potential energy curves for the nonequivalent atoms in Mg_3Sb_2 displacing along the *a* and *c* directions. **c**, **d** are reproduced with permissions from ref. [79], CC-BY-4.0

are mainly contributed by the motion of Mg1 while the acoustic phonon modes are dominated by the vibration of Sb (Fig. 10b, c). It is more likely that the unstable or weak chemical bonds lead to the soft transverse acoustic phonon modes in Mg_3Sb_2 and Mg_3Bi_2.

The soft transverse acoustic phonon modes in Mg_3Sb_2 and Mg_3Bi_2 involve the interlayer shearing motion, which results in their reported soft shear moduli.[82,97] However, whether the soft shear modes are mainly induced by the weak interlayer Mg1-Sb (or Mg1-Bi) bond requires further confirmation. Quantitative chemical bonding analysis based on the electron density[98] is reliable in comparing different chemical bonds in the same compound, but it cannot be used for reliably comparing the relative strength of chemical bonds in different compounds. Therefore, other computational methods should be applied to quantitatively characterize and compare the relative strength of the interlayer A-X bonds in different compounds. Furthermore, other factors such as the difference in atomic masses should also be considered. Overall, more comprehensive work should be conducted in the future to reveal the origin of these unique soft transverse modes in Mg_3Sb_2 and Mg_3Bi_2.

ELECTRONIC AND THERMAL TRANSPORT ANISOTROPY

Experimentally, the anisotropy of the transport properties in bulk TE materials can vary a lot between different reports[48,102,130,143] since it is sensitive to the factors such as the sample quality, crystal alignment, and preferred orientations. Therefore, here we will focus on the anisotropy of electrical and thermal transport based on the perfect crystal structure from the theoretical point of view. In general, only electronic states near the Fermi level contribute to the electronic transport. Under the constant and isotropic carrier scattering time assumption, the anisotropy of electrical conductivity is completely determined by the anisotropy in carrier mobility and thereby the anisotropy in the inverse effective mass tensor, which can be intuitively understood from the anisotropy of the atomic orbitals interactions. For p-type transport in Mg_3Sb_2, the electronic states at the VBM are mainly comprised of the p_z orbitals of the Sb atoms.[105] The anisotropic p_z orbitals show much stronger orbital overlaps along the *c* axis, which results in much larger band dispersion, smaller effective mass, and larger electrical conductivity in comparison to those along the *a* axis. This is confirmed by the calculated strong anisotropy in the electrical conductivity for p-type Mg_3Sb_2 with σ_{xx}/σ_{zz} being much smaller than unity (see Fig. 12a), consistent with the experimental reports.[102] In contrast, for n-type transport in Mg_3Sb_2, the electronic states at the CBM are dominated by spherical *s* orbitals of the Mg atoms,[55,57] which generally result in nearly isotropic features in orbital interactions, average effective mass tensor, and thereby electrical conductivity (Fig. 12a).[144] For the Seebeck coefficient, both p-type and n-type Mg_3Sb_2 show a nearly isotropic

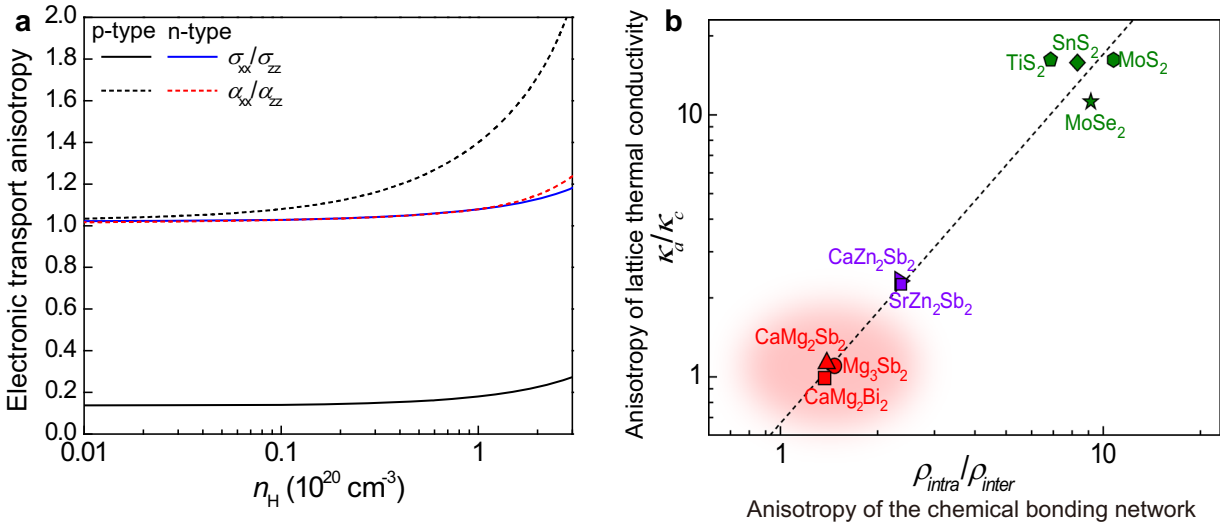

Fig. 12 **a** Anisotropy of the calculated electronic transport properties including Seebeck coefficient (α_{xx}/α_{zz}) and electrical conductivity (σ_{xx}/σ_{zz}) as a function of Hall carrier concentration in p-type and n-type Mg_3Sb_2. The data are calculated in this work using the previous computational methods[54]. **b** Anisotropy of the theoretical lattice thermal conductivity κ_a/κ_c as a function of the anisotropy of the chemical bonding network characterized by $\rho_{intra}/\rho_{inter}$. **b** is reproduced with permissions from ref. [79], CC-BY-4.0

feature even though the effective mass tensor is anisotropic (Fig. 12a). This may be attributed to the notion, which was proposed by Parker et al.,[114] that the anisotropic effective mass results in isotropic Seebeck coefficient as long as the electronic band is assumed parabolic, the carrier scattering time is assumed only dependent on energy, and the bipolar effect is insignificant. Moreover, as investigated by Sun et al.,[117] the Seebeck coefficients of several ternary compounds AMg_2X_2 and AZn_2Sb_2 (A = Ca, Sr, Ba; X = Sb, Bi) also show isotropic features when there is no bipolar effect, whereas the n-type electrical conductivities in these compounds show anisotropic features due to the anisotropic average effective mass tensors induced by the anisotropic electron pockets, which may be understood from the anisotropic orbital interactions induced by the increased contributions of anisotropic *p* and *d* orbitals to the CBM.

In general, the thermal transport anisotropy is related to the anisotropy of the chemical bonding network.[79,145] In Mg_3Sb_2 and related structures, the anisotropy of the chemical bonding network can be quantified by the intralayer-to-interlayer bond-strength ratio $\rho_{intra}/\rho_{inter}$ based on electron density.[79] A nearly linear correlation between the anisotropy ratio κ_a/κ_c of lattice thermal conductivity and $\rho_{intra}/\rho_{inter}$ indicates that $\rho_{intra}/\rho_{inter}$ can be adopted as an indicator measuring the anisotropy of lattice thermal conductivity in Mg_3Sb_2-related materials (see Fig. 12b). For AMg_2X_2 compounds, the nearly isotropic 3D bonding network with $\rho_{intra}/\rho_{inter} \approx 1$ results in the nearly isotropic features in phonon dispersion, group velocity, Grüneisen parameter, and ultimately lattice thermal conductivity.[79] However, the lattice thermal conductivity in AZn_2Sb_2 is relatively anisotropic due to the anisotropic chemical bonding network with $\rho_{intra}/\rho_{inter} > 2$.

SUMMARY AND OUTLOOK

In this review, we have explored many illuminating insights such as orbital overlap, orbital degeneracy, orbital splitting energy, valley degeneracy, effective mass, carrier pocket anisotropy, Fermi surface complexity, point defects, electronegativity, and bond covalency for understanding electronic and thermal transport of Mg_3Sb_2 and related $CaAl_2Si_2$-type TEs. Although current insights for the materials design have been very helpful to date, many challenges need to be addressed in order to achieve further development. Below we present some challenges and possible future directions in both theoretical and experimental aspects.

Theoretically, critical challenges include the difficulties for current computations to describe the carrier scattering time, doping, temperature effects, defects, and disorder in experiments. One typical example of these challenges can be seen in electrical transport calculations under the rigid band and constant carrier's scattering time approximation, which assumes electronic bands and scattering time being insensitive to temperature and doping. In reality, doping on the cation sites and varying carrier scattering mechanisms result in the deviation from theory and the scatter of experimental data in the Pisarenko plot of the Seebeck coefficient versus carrier density (see Fig. 6d). Another example can be found in the situation where the high carrier mobility cannot be understood from the band structure. In several compounds containing rare earth elements, the carrier's scattering time is responsible for the intrinsically high carrier mobility, whereas the detailed mechanism requires further investigation. In n-type $Mg_3Sb_{2-x}Bi_x$, changing carrier scattering behavior can improve carrier mobility by doping with transition metals on the Mg sites or increasing the pressing temperature, but the underlying mechanism is still under debate.

In addition, the insights into the origin of valence and conduction band alignments, how thermal expansion affects band alignments, and the origin of carrier pocket anisotropy remain unclear. The underlying mechanism on why the favorable six-fold CBM at the low-symmetry CB_1 point only exists in binary Mg_3X_2 requires further investigation. For defect calculations, more potential n-type dopants need to be predicted for the experimental validations. Regarding thermal transport, further efforts are required to elucidate the origin of the soft transverse acoustic phonon modes in Mg_3Sb_2 and Mg_3Bi_2 that remains obscurely understood to date. Whether the soft transverse acoustic modes are induced by the weak interlayer interaction should be carefully examined. The critical challenge here for computations is how to quantitatively and reliably compare the strength of interlayer interactions in different compounds. In addition to this possible notion, the impact of other factors such as the atomic mass difference on phonon transport should be examined.

Experimentally, the reported compositions are mainly limited to Sb- and Bi-based compounds, while As- and P-based compounds remain largely unexplored. According to the solid solution compound map, there are still many unexplored alloying

combinations showing the potential to achieve superior p-type electrical properties with minimal crystal orbital splitting energy values. Moreover, excellent n-type properties have only been discovered in $Mg_3Sb_{2-x}Bi_x$ with few effective electron dopants such as the chalcogens, Y, and La. Hence, other effective n-type dopants for $Mg_3Sb_{2-x}Bi_x$ as well as other potential material systems such as $Mg_3Sb_{2-x}As_x$ and $Mg_3Bi_{2-x}As_x$ for n-type doping need to be explored in the future. Despite the outstanding TE performance shown in n-type Mg_3Sb_2-based materials, the long-term thermal stability under a temperature gradient and an electrical current should be addressed as an essential step toward the practical applications.

ACKNOWLEDGEMENTS

We thank K.F.F. Fischer for discussions and comments. This work was supported by the Danish National Research Foundation (Center for Materials Crystallography, DNRF93) and the Danish Center for Scientific Computing. The numerical results presented in this work were obtained at the Center for Scientific Computing, Aarhus. Affiliation with the Center for Integrated Materials Research (iMAT) at Aarhus University is gratefully acknowledged.

AUTHOR CONTRIBUTIONS

J.Z. wrote the manuscript with the inputs and suggestions from B.B.I. L.S. collected the reported experimental data and edited the manuscript.

ADDITIONAL INFORMATION

Competing interests: The authors declare no competing interests.

Publisher's note: Springer Nature remains neutral with regard to jurisdictional claims in published maps and institutional affiliations.

REFERENCES

1. Goldsmid, H. J. *Thermoelectric Refrigeration* (Plenum, New York, 1964).
2. Nolas, G. S, Sharp, J. & Goldsmid, H. J. *Thermoelectrics: Basic Principles and New Materials Developments* (Springer, New York, 2001).
3. Snyder, G. J., Christensen, M., Nishibori, E., Caillat, T. & Iversen, B. B. Disordered zinc in Zn_4Sb_3 with phonon-glass and electron-crystal thermoelectric properties. *Nat. Mater.* **3**, 458–463 (2004).
4. Zaitsev, V. K. et al. Highly effective $Mg_2Si_{1-x}Sn_x$ thermoelectrics. *Phys. Rev. B* **74**, 045207 (2006).
5. Christensen, M. et al. Avoided crossing of rattler modes in thermoelectric materials. *Nat. Mater.* **7**, 811–815 (2008).
6. Pei, Y. et al. Convergence of electronic bands for high performance bulk thermoelectrics. *Nature* **473**, 66–69 (2011).
7. Biswas, K. et al. High-performance bulk thermoelectrics with all-scale hierarchical architectures. *Nature* **489**, 414–418 (2012).
8. Liu, H. et al. Copper ion liquid-like thermoelectrics. *Nat. Mater.* **11**, 422–425 (2012).
9. Zhang, J. et al. High-performance pseudocubic thermoelectric materials from non-cubic chalcopyrite compounds. *Adv. Mater.* **26**, 3848–3853 (2014).
10. Zhao, L.-D. et al. Ultralow thermal conductivity and high thermoelectric figure of merit in SnSe crystals. *Nature* **508**, 373–377 (2014).
11. Zheng, C. & Hoffmann, R. Complementary local and extended views of bonding in the $ThCr_2Si_2$ and $CaAl_2Si_2$ structures. *J. Solid State Chem.* **72**, 58–71 (1988).
12. Zheng, C., Hoffmann, R., Nesper, R. & Von Schnering, H. G. Site preferences and bond length differences in $CaAl_2Si_2$-type Zintl compounds. *J. Am. Chem. Soc.* **108**, 1876–1884 (1986).
13. Verbrugge, D. M. & Zytveld, J. B. J. V. Electronic properties of liquid MgSb. *J. Non-Cryst. Solids* **156–158**, 736 (1993).
14. Stark, D. & Snyder, G. J. The synthesis of $CaZn_2Sb_2$ and its thermoelectric properties. In *Proc. 21th Inter. Conf. Thermoelectrics* 181–184 (Institute of Electrical and Electronics Engineers Inc., Piscataway, NJ, 2002).
15. Gascoin, F., Ottensmann, S., Stark, D., Haïle, S. M. & Snyder, G. J. Zintl phases as thermoelectric materials: tuned transport properties of the compounds $Ca_xYb_{1-x}Zn_2Sb_2$. *Adv. Funct. Mater.* **15**, 1860–1864 (2005).
16. Yu, C. et al. Improved thermoelectric performance in the Zintl phase compounds $YbZn_{2-x}Mn_xSb_2$ via isoelectronic substitution in the anionic framework. *J. Appl. Phys.* **104**, 013705 (2008).
17. Zhang, H. et al. A new type of thermoelectric material, $EuZn_2Sb_2$. *J. Chem. Phys.* **129**, 164713 (2008).
18. Wang, X.-J. et al. Synthesis and high thermoelectric efficiency of Zintl phase $YbCd_{2-x}Zn_xSb_2$. *Appl. Phys. Lett.* **94**, 092106 (2009).
19. Cao, Q.-G. et al. Zintl phase $Yb_{1-x}Ca_xCd_2Sb_2$ with tunable thermoelectric properties induced by cation substitution. *J. Appl. Phys.* **107**, 053714 (2010).
20. Toberer, E. S., May, A. F., Melot, B. C., Flage-Larsen, E. & Snyder, G. J. Electronic structure and transport in thermoelectric compounds AZn_2Sb_2 (A=Sr, Ca, Yb, Eu). *Dalton Trans.* **39**, 1046–1054 (2010).
21. Zhang, H. et al. Thermoelectric properties of $Eu(Zn_{1-x}Cd_x)_2Sb_2$. *Dalton Trans.* **39**, 1101–1104 (2010).
22. Zhang, H. et al. Synthesis and properties of $CaCd_2Sb_2$ and $EuCd_2Sb_2$. *Intermetallics* **18**, 193–198 (2010).
23. Zhang, H. et al. Thermoelectric properties of $Yb_xEu_{1-x}Cd_2Sb_2$. *J. Chem. Phys.* **133**, 194701 (2010).
24. Zhang, H. et al. Thermoelectric properties of polycrystalline $SrZn_2Sb_2$ prepared by spark plasma sintering. *J. Electron. Mater.* **39**, 1772–1776 (2010).
25. Guo, K. et al. Enhanced thermoelectric figure of merit of Zintl phase $YbCd_{2-x}Mn_xSb_2$ by chemical substitution. *Eur. J. Inorg. Chem.* **2011**, 4043–4048 (2011).
26. May, A. F. et al. Thermoelectric transport properties of $CaMg_2Bi_2$, $EuMg_2Bi_2$, and $YbMg_2Bi_2$. *Phys. Rev. B* **85**, 035202 (2012).
27. Zevalkink, A. et al. Nonstoichiometry in the Zintl phase $Yb_{1-\delta}Zn_2Sb_2$ as a route to thermoelectric optimization. *Chem. Mater.* **26**, 5710–5717 (2014).
28. Min, W., Guo, K., Wang, J. & Zhao, J. Effect of manganese doping on the thermoelectric properties of Zintl phase $EuCd_2Sb_2$. *J. Rare Earth.* **33**, 1093–1097 (2015).
29. Shuai, J. et al. Higher thermoelectric performance of Zintl phases $(Eu_{0.5}Yb_{0.5})_{1-x}Ca_xMg_2Bi_2$ by band engineering and strain fluctuation. *Proc. Natl Acad. Sci. USA* **113**, E4125–E4132 (2016).
30. Shuai, J. et al. Thermoelectric properties of Zintl compound $Ca_{1-x}Na_xMg_2Bi_{1.98}$. *Appl. Phys. Lett.* **108**, 183901 (2016).
31. Shuai, J. et al. Thermoelectric properties of Bi-based Zintl compounds $Ca_{1-x}Yb_xMg_2Bi_2$. *J. Mater. Chem. A* **4**, 4312–4320 (2016).
32. Wubieneh, T. A., Wei, P.-C., Yeh, C.-C., Chen, S.-y & Chen, Y.-Y. Thermoelectric properties of Zintl phase compounds of $Ca_{1-x}Eu_xZn_2Sb_2$ ($0 \le x \le 1$). *J. Electron. Mater.* **45**, 1942–1946 (2016).
33. Takagiwa, Y. et al. Thermoelectric properties of $EuZn_2Sb_2$ Zintl compounds: zT enhancement through Yb substitution for Eu. *J. Alloy. Compd.* **703**, 73–79 (2017).
34. Wang, X. et al. Single parabolic band transport in p-type $EuZn_2Sb_2$ thermoelectrics. *J. Mater. Chem. A* **5**, 24185–24192 (2017).
35. Wang, X. et al. Orbital alignment for high performance thermoelectric $YbCd_2Sb_2$ alloys. *Chem. Mater.* **30**, 5339–5345 (2018).
36. Wood, M., Aydemir, U., Ohno, S. & Snyder, G. J. Observation of valence band crossing: the thermoelectric properties of $CaZn_2Sb_2$–$CaMg_2Sb_2$ solid solution. *J. Mater. Chem. A* **6**, 9437–9444 (2018).
37. Kunioka, H. et al. Thermoelectric properties of $(Ba,K)Cd_2As_2$ crystallized in the $CaAl_2Si_2$-type structure. *Dalton Trans.* **47**, 16205–16210 (2018).
38. Kajikawa, T., Kimura, N. & Yokoyama, T. Thermoelectric properties of intermetallic compounds: Mg_3Bi_2 and Mg_3Sb_2 for medium temperature range thermoelectric elements. In *Proc. 22th Inter. Conf. Thermoelectrics* 305–308 (Institute of Electrical and Electronics Engineers Inc., Piscataway, NJ, 2003).
39. Condron, C. L., Kauzlarich, S. M., Gascoin, F. & Snyder, G. J. Thermoelectric properties and microstructure of Mg_3Sb_2. *J. Solid State Chem.* **179**, 2252–2257 (2006).
40. Bhardwaj, A. et al. Mg_3Sb_2-based Zintl compound: a non-toxic, inexpensive and abundant thermoelectric material for power generation. *RSC Adv.* **3**, 8504–8516 (2013).
41. Ponnambalam, V. & Morelli, D. On the thermoelectric properties of Zintl compounds $Mg_3Bi_{2-x}Pn_x$ (Pn=P and Sb). *J. Electron. Mater.* **42**, 1307–1312 (2013).
42. Bhardwaj, A. & Misra, D. K. Enhancing thermoelectric properties of a p-type Mg_3Sb_2-based Zintl phase compound by Pb substitution in the anionic framework. *RSC Adv.* **4**, 34552–34560 (2014).
43. Bhardwaj, A., Chauhan, N. S. & Misra, D. K. Significantly enhanced thermoelectric figure of merit of p-type Mg_3Sb_2-based Zintl phase compounds via nanostructuring and employing high energy mechanical milling coupled with spark plasma sintering. *J. Mater. Chem. A* **3**, 10777–10786 (2015).
44. Bhardwaj, A., Shukla, A. K., Dhakate, S. R. & Misra, D. K. Graphene boosts thermoelectric performance of a Zintl phase compound. *RSC Adv.* **5**, 11058–11070 (2015).
45. Shuai, J. et al. Thermoelectric properties of Na-doped Zintl compound: $Mg_{3-x}Na_xSb_2$. *Acta Mater.* **93**, 187–193 (2015).
46. Song, L., Zhang, J. & Iversen, B. B. Simultaneous improvement of power factor and thermal conductivity via Ag doping in p-type Mg_3Sb_2 thermoelectric materials. *J. Mater. Chem. A* **5**, 4932–4939 (2017).

47. Chen, C. et al. Enhanced thermoelectric performance of p-type Mg_3Sb_2 by lithium doping and its tunability in an anionic framework. *J. Mater. Sci.* **53**, 16001–16009 (2018).
48. Lv, F. et al. Isotropic Mg_3Sb_2 compound prepared by solid-state reaction and ball milling combined with spark plasma sintering. *J. Mater. Sci.* **53**, 8039–8048 (2018).
49. Ren, Z. S. et al. Significantly enhanced thermoelectric properties of p-type Mg_3Sb_2 via co-doping of Na and Zn. *Acta Mater.* **143**, 265–271 (2018).
50. Wang, H. et al. Enhanced thermoelectric performance in p-type Mg_3Sb_2 via lithium doping. *Chin. Phys. B* **27**, 047212 (2018).
51. Kim, S. et al. Thermoelectric properties of Mn-doped Mg-Sb single crystals. *J. Mater. Chem. A* **2**, 12311–12316 (2014).
52. Bhardwaj, A. et al. Tuning the carrier concentration using Zintl chemistry in Mg_3Sb_2, and its implications for thermoelectric figure-of-merit. *Phys. Chem. Chem. Phys.* **18**, 6191–6200 (2016).
53. Pedersen, S. H. *Thermoelectric Properties of Zintl Compounds* $Mg_3Sb_{2-x}Bi_x$. (Chemistry Project for Master's Degree, Department of Chemistry, Aarhus University, 2012). The thesis is available at http://chem.au.dk/fileadmin/cmc.chem.au.dk/pictures_new_homepage/Pedersen_S_H_-_Thermoelectric_Properties_of_Zintl_Compounds_Mg3Sb2-xBix.pdf.
54. Zhang, J. et al. Discovery of high-performance low-cost n-type Mg_3Sb_2-based thermoelectric materials with multi-valley conduction bands. *Nat. Commun.* **8**, 13901 (2017).
55. Tamaki, H., Sato, H. K. & Kanno, T. Isotropic conduction network and defect chemistry in $Mg_{3+\delta}Sb_2$-based layered Zintl compounds with high thermoelectric performance. *Adv. Mater.* **28**, 10182–10187 (2016).
56. Shuai, J. et al. Tuning the carrier scattering mechanism to effectively improve the thermoelectric properties. *Energy Environ. Sci.* **10**, 799–807 (2017).
57. Zhang, J., Song, L., Mamakhel, A., Jørgensen, M. R. V. & Iversen, B. B. High-performance low-cost n-type Se-doped Mg_3Sb_2-based Zintl compounds for thermoelectric application. *Chem. Mater.* **29**, 5371–5383 (2017).
58. Mao, J. et al. Manipulation of ionized impurity scattering for achieving high thermoelectric performance in n-type Mg_3Sb_2-based materials. *Proc. Natl Acad. Sci. USA* **114**, 10548–10553 (2017).
59. Mao, J. et al. Defect engineering for realizing high thermoelectric performance in n-type Mg_3Sb_2-based materials. *ACS Energy Lett.* **2**, 2245–2250 (2017).
60. Zhang, J., Song, L., Borup, K. A., Jørgensen, M. R. V. & Iversen, B. B. New insight on tuning electrical transport properties via chalcogen doping in n-type Mg_3Sb_2-based thermoelectric materials. *Adv. Energy Mater.* **8**, 1702776 (2018).
61. Ohno, S. et al. Phase boundary mapping to obtain n-type Mg_3Sb_2-based thermoelectrics. *Joule* **2**, 141–154 (2018).
62. Imasato, K., Kang, S. D., Ohno, S. & Snyder, G. J. Band engineering in Mg_3Sb_2 by alloying with Mg_3Bi_2 for enhanced thermoelectric performance. *Mater. Horiz.* **5**, 59–64 (2018).
63. Imasato, K., Ohno, S., Kang, S. D. & Snyder, G. J. Improving the thermoelectric performance in $Mg_{3+x}Sb_{1.5}Bi_{0.49}Te_{0.01}$ by reducing excess Mg. *APL Mater.* **6**, 016106 (2018).
64. Kanno, T. et al. Enhancement of average thermoelectric figure of merit by increasing the grain-size of $Mg_{3.2}Sb_{1.5}Bi_{0.49}Te_{0.01}$. *Appl. Phys. Lett.* **112**, 033903 (2018).
65. Shuai, J. et al. Significant role of Mg stoichiometry in designing high thermoelectric performance for $Mg_3(Sb,Bi)_2$-based n-type Zintls. *J. Am. Chem. Soc.* **140**, 1910–1915 (2018).
66. Chen, X. et al. Extraordinary thermoelectric performance in n-type manganese doped Mg_3Sb_2 Zintl: High band degeneracy, tuned carrier scattering mechanism and hierarchical microstructure. *Nano Energy* **52**, 246–255 (2018).
67. Imasato, K., Wood, M., Kuo, J. J. & Snyder, G. J. Improved stability and high thermoelectric performance through cation site doping in n-type La-doped $Mg_3Sb_{1.5}Bi_{0.5}$. *J. Mater. Chem. A* **6**, 19941–19946 (2018).
68. Shu, R. et al. $Mg_{3+\delta}Sb_xBi_{2-x}$ family: a promising substitute for the state-of-the-art n-type thermoelectric materials near room temperature. *Adv. Funct. Mater.* **29**, 1807235 (2019).
69. Song, S. W. et al. Joint effect of magnesium and yttrium on enhancing thermoelectric properties of n-type Zintl $Mg_{3+\delta}Y_{0.02}Sb_{1.5}Bi_{0.5}$. *Mater. Today Phys.* **8**, 25–33 (2019).
70. Imasato, K., Kang, S. D. & Snyder, G. J. Exceptional thermoelectric performance in $Mg_3Sb_{0.6}Bi_{1.4}$ for low-grade waste heat recovery. *Energy Environ. Sci.* **12**, 965–971 (2019).
71. Chen, X. et al. Porosity-mediated high-performance thermoelectric Materials. Preprint at https://arxiv.org/abs/1810.03356 (2018).
72. Jørgensen, L. R., Zhang, J. W., Zeuthen, C. B. & Iversen, B. B. Thermal stability of $Mg_3Sb_{1.475}Bi_{0.475}Te_{0.05}$ high performance n-type thermoelectric investigated through powder X-ray diffraction and pair distribution function analysis. *J. Mater. Chem. A* **6**, 17171–17176 (2018).
73. Song, L., Zhang, J. & Iversen, B. B. Thermal stability of p-type Ag-doped Mg_3Sb_2 thermoelectric materials investigated by powder X-ray diffraction. *Phys. Chem. Chem. Phys.* **21**, 4295–4305 (2019).
74. Singh, D. J. & Parker, D. Electronic and transport properties of zintl phase $AeMg_2Pn_2$, Ae=Ca,Sr,Ba, Pn=As,Sb,Bi in relation to Mg_3Sb_2. *J. Appl. Phys.* **114**, 143703 (2013).
75. Watson, L. M., Marshall, C. A. W. & Cardoso, C. P. On the electronic structure of the semiconducting compounds Mg_3Bi_2 and Mg_3Sb_2. *J. Phys. F: Met. Phys.* **14**, 113 (1984).
76. Xu, R., Groot, R. Ad & Lugt, Wvd Resistivities and band structures of alkaline-earth-pnictide systems. *J. Phys. Condens. Matter* **5**, 7551 (1993).
77. Imai, Y. & Watanabe, A. Electronic structures of Mg_3Pn_2 (Pn=N, P, As, Sb and Bi) and Ca_3N_2 calculated by a first-principle pseudopotential method. *J. Mater. Sci.* **41**, 2435–2441 (2006).
78. Burdett, J. K. & Miller, G. J. Fragment formalism in main-group solids: applications to aluminum boride (AlB_2), calcium aluminum silicide ($CaAl_2Si_2$), barium-aluminum ($BaAl_4$), and related materials. *Chem. Mater* **2**, 12–26 (1990).
79. Zhang, J., Song, L., Sist, M., Tolborg, K. & Iversen, B. B. Chemical bonding origin of the unexpected isotropic physical properties in thermoelectric Mg_3Sb_2 and related materials. *Nat. Commun.* **9**, 4716 (2018).
80. Pomrehn, G. S., Zevalkink, A., Zeier, W. G., van de Walle, A. & Snyder, G. J. Defect-controlled electronic properties in AZn_2Sb_2 Zintl phases. *Angew. Chem. Int. Ed.* **53**, 3422–3426 (2014).
81. Tani, J.-i, Takahashi, M. & Kido, H. Lattice dynamics and elastic properties of Mg_3As_2 and Mg_3Sb_2 compounds from first-principles calculations. *Phys. B* **405**, 4219–4225 (2010).
82. Peng, W., Petretto, G., Rignanese, G. M., Hautier, G. & Zevalkink, A. An unlikely route to low lattice thermal conductivity: small atoms in a simple layered structure. *Joule* **2**, 1879–1893 (2018).
83. Maccioni, M. B., Farris, R. & Fiorentini, V. Ab initio thermal conductivity of thermoelectric Mg_3Sb_2: evidence for dominant extrinsic effects. *Phys. Rev. B* **98**, 220301(R) (2018).
84. Zhang, J. & Iversen, B. B. Lattice dynamics and lattice thermal conductivity of Mg_3Sb_2, in preparation (2019).
85. Gladyshevskii, E. I., Krypyakevych, P. I. & Bodak, O. I. The crystal structure of the compound $CaAl_2Si_2$ and its analogues. *Ukr. Fiz. Zh.* **12**, 447–452 (1967).
86. Martinez-Ripoll, M., Haase, A. & Brauer, G. The crystal structure of α-Mg_3Sb_2. *Acta Cryst. B* **30**, 2006–2009 (1974).
87. Zintl, E. & Husemann, E. Bindungsart und gitterbau binärer magnesiumverbindungen. *Z. Phys. Chem.* **21B**, 138–155 (1933).
88. Grube, G. & Bornhak, R. Das Zustandsdiagramm magnesium-antimon. *Z. Elektrochem.* **40**, 140–142 (1934).
89. Grube, G., Mohr, L. & Bornhak, R. Elektrische leitfähigkeit und zustandsdiagramm bei binären legierungen. 10. mitteilung. Das system magnesium-wismut. *Z. Elektrochem.* **40**, 143–150 (1934).
90. Barnes, A. C., Guo, C. & Howells, W. S. Fast-ion conduction and the structure of β-Mg_3Bi_2. *J. Phys. Condens. Matter* **6**, L467–L471 (1994).
91. Zintl, E. Intermetallische verbindungen. *Angew. Chem.* **52**, 1–6 (1939).
92. Schäfer, H., Eisenmann, B. & Müller, W. Zintl phases: transitions between metallic and ionic bonding. *Angew. Chem. Int. Ed.* **12**, 694–712 (1973).
93. Kauzlarich, S. M., Brown, S. R. & Jeffrey Snyder, G. Zintl phases for thermoelectric devices. *Dalton Trans.* **0**, 2099–2107 (2007).
94. Snyder, G. J. & Toberer, E. S. Complex thermoelectric materials. *Nat. Mater.* **7**, 105–114 (2008).
95. May, A. F. et al. Properties of single crystalline AZn_2Sb_2 (A=Ca,Eu,Yb). *J. Appl. Phys.* **111**, 033708 (2012).
96. Alemany, P., Llunell, M. & Canadell, E. Roles of cations, electronegativity difference, and anionic interlayer interactions in the metallic versus nonmetallic character of Zintl phases related to arsenic. *J. Comput. Chem.* **29**, 2144–2153 (2008).
97. Li, G. et al. Deformation mechanisms in high-efficiency thermoelectric layered Zintl compounds. *J. Mater. Chem. A* **5**, 9050–9059 (2017).
98. Bader, R. F. W. *Atoms in Molecules: A Quantum Theory* (Oxford University Press, Oxford, 1990).
99. Mori-Sánchez, P., Pendás, A. M. & Luaña, V. A classification of covalent, ionic, and metallic solids based on the electron density. *J. Am. Chem. Soc.* **124**, 14721–14723 (2002).
100. Gatti, C. Chemical bonding in crystals: new directions. *Z. Krist.* **220**, 399–457 (2005).
101. Johnson, E. R. et al. Revealing noncovalent interactions. *J. Am. Chem. Soc.* **132**, 6498–6506 (2010).
102. Soo Hyun, K. et al. Thermoelectric properties of $Mg_3Sb_{2-x}Bi_x$ single crystals grown by Bridgman method. *Mater. Res. Express* **2**, 055903 (2015).
103. Goldsmid, H. J. *Introduction to Thermoelectricity* (Springer, Berlin, 2009).

104. Liu, W. et al. Convergence of conduction bands as a means of enhancing thermoelectric performance of n-type $Mg_2Si_{1-x}Sn_x$ solid solutions. *Phys. Rev. Lett.* **108**, 166601 (2012).
105. Zhang, J. et al. Designing high-performance layered thermoelectric materials through orbital engineering. *Nat. Commun.* **7**, 10892 (2016).
106. Cox, P. A. *The Electronic Structure and Chemistry of Solids* (Oxford University Press, Oxford, 1987).
107. Peng, W., Chanakian, S. & Zevalkink, A. Crystal chemistry and thermoelectric transport of layered AM_2X_2 compounds. *Inorg. Chem. Front.* **5**, 1744–1759 (2018).
108. Perdew, J. P., Burke, K. & Ernzerhof, M. Generalized gradient approximation made simple. *Phys. Rev. Lett.* **77**, 3865–3868 (1996).
109. Perdew, J. P. & Zunger, A. Self-interaction correction to density-functional approximations for many-electron systems. *Phys. Rev. B* **23**, 5048–5079 (1981).
110. Tran, F. & Blaha, P. Accurate band gaps of semiconductors and insulators with a semilocal exchange-correlation potential. *Phys. Rev. Lett.* **102**, 226401 (2009).
111. Li, J. et al. Designing high-performance n-type Mg_3Sb_2-based thermoelectric materials through forming solid solutions and biaxial strain. *J. Mater. Chem. A* **6**, 20454–20462 (2018).
112. Gibbs, Z. M. et al. Effective mass and Fermi surface complexity factor from ab initio band structure calculations. *npj Comput. Mater* **3**, 8 (2017).
113. Zhang, J. & Iversen, B. B. Fermi surface complexity, effective mass, and conduction band alignment in n-type thermoelectric $Mg_3Sb_{2-x}Bi_x$ from first principles calculations. Preprint at https://arxiv.org/abs/1907.02263 (2019).
114. Parker, D. S., May, A. F. & Singh, D. J. Benefits of carrier-pocket anisotropy to thermoelectric performance: the case of p-type $AgBiSe_2$. *Phys. Rev. Appl.* **3**, 064003 (2015).
115. Madsen, G. K. H. & Singh, D. J. BoltzTraP. A code for calculating band-structure dependent quantities. *Comput. Phys. Commun.* **175**, 67–71 (2006).
116. Lykke, L., Iversen, B. B. & Madsen, G. K. H. Electronic structure and transport in the low-temperature thermoelectric $CsBi_4Te_6$: Semiclassical transport equations. *Phys. Rev. B* **73**, 195121 (2006).
117. Sun, J. & Singh, D. J. Thermoelectric properties of AMg_2X_2, AZn_2Sb_2 (A=Ca, Sr, Ba; X=Sb, Bi), and Ba_2ZnX_2 (X=Sb, Bi) Zintl compounds. *J. Mater. Chem. A* **5**, 8499–8509 (2017).
118. Sun, X. et al. Achieving band convergence by tuning the bonding ionicity in n-type Mg_3Sb_2. *J. Comput. Chem.* **40**, 1693–1700 (2019).
119. Mahan, G. D. & Sofo, J. O. The best thermoelectric. *Proc. Natl Acad. Sci. USA* **93**, 7436–7439 (1996).
120. Kuo, J. J. et al. Grain boundary dominated charge transport in Mg_3Sb_2-based compounds. *Energy Environ. Sci.* **11**, 429–434 (2018).
121. Chong, X. et al. Understanding the intrinsic p-type behavior and phase stability of thermoelectric α-Mg_3Sb_2. *ACS Appl. Energy Mater.* **1**, 6600–6608 (2018).
122. Lee, K., Bux, S. K. & Fleurial, J.-P. *Thermal stability and transport properties of n-type* $Mg_3Sb_{2-x}Bi_x$. Poster presented at 36th Inter. Conf. Thermoelectrics, Pasadena, CA, USA (2017).
123. Imai, M., Abe, H. & Yamada, K. Electrical properties of single-crystalline $CaAl_2Si_2$. *Inorg. Chem.* **43**, 5186–5188 (2004).
124. Kauzlarich, S. M., Condron, C. L., Wassei, J. K., Ikeda, T. & Snyder, G. J. Structure and high-temperature thermoelectric properties of $SrAl_2Si_2$. *J. Solid State Chem.* **182**, 240–245 (2009).
125. Bjerg, L., Madsen, G. K. H. & Iversen, B. B. Ab initio calculations of intrinsic point defects in ZnSb. *Chem. Mater.* **24**, 2111–2116 (2012).
126. Xin, H. X. & Qin, X. Y. Electrical and thermoelectric properties of nanocrystal substitutional semiconductor alloys $Mg_3(Bi_xSb_{1-x})_2$ prepared by mechanical alloying. *J. Phys. D Appl. Phys.* **39**, 5331 (2006).
127. Xin, H. X., Qin, X. Y., Zhu, X. G. & Liu, Y. Temperature dependence of electrical resistivity for nanocrystalline $Mg_{3+x}Sb_2$ prepared by mechanical alloying. *J. Phys. D Appl. Phys.* **39**, 375 (2006).
128. Ahmadpour, F., Kolodiazhnyi, T. & Mozharivskyj, Y. Structural and physical properties of $Mg_{3-x}Zn_xSb_2$ (x=0–1.34). *J. Solid State Chem.* **180**, 2420–2428 (2007).
129. Zhang, K. X., Qin, X. Y., Xin, H. X., Li, H. J. & Zhang, J. Transport and thermoelectric properties of nanocrystal substitutional semiconductor alloys $(Mg_{1-x}Cd_x)_3Sb_2$ doped with Ag. *J. Alloy. Compd.* **484**, 498–504 (2009).
130. Xin, J. et al. Growth and transport properties of Mg_3X_2 (X=Sb, Bi) single crystals. *Mater. Today Phys.* **7**, 61–68 (2018).
131. Paier, J. et al. Screened hybrid density functionals applied to solids. *J. Chem. Phys.* **124**, 154709 (2006).
132. Allred, A. L. & Rochow, E. G. A scale of electronegativity based on electrostatic force. *J. Inorg. Nucl. Chem.* **5**, 264–268 (1958).
133. Pauling, L. The nature of the chemical bond. IV. The energy of single bonds and the relative electronegativity of atoms. *J. Am. Chem. Soc.* **54**, 3570–3582 (1932).
134. Slack, G. A. in *CRC Handbook of Thermoelectrics* (ed. Rowe, D. M.) 407 (CRC, Boca Raton, FL, 1995).
135. Zeier, W. G. et al. Thinking like a chemist: intuition in thermoelectric materials. *Angew. Chem. Int. Ed.* **55**, 6826–6841 (2016).
136. Gorai, P., Ortiz, B. R., Toberer, E. S. & Stevanovic, V. Investigation of n-type doping strategies for Mg_3Sb_2. *J. Mater. Chem. A* **6**, 13806–13815 (2018).
137. Gorai, P., Toberer, E. S. & Stevanović, V. Effective n-type doping of Mg_3Sb_2 with group-3 elements. *J. Appl. Phys.* **125**, 025105 (2019).
138. Ravich, Y. I., Efimova, B. A. & Smirnov, I. A. *Semiconducting Lead Chalcogenides* (Plenum Press, New York, 1970).
139. Rowe, D. M. (ed.) *CRC Handbook of Thermoelectrics* (CRC, Boca Raton, FL, 1995).
140. Li, W., Carrete, J., A. Katcho, N. & Mingo, N. ShengBTE: a solver of the Boltzmann transport equation for phonons. *Comput. Phys. Commun.* **185**, 1747–1758 (2014).
141. Jain, A. et al. The Materials Project: a materials genome approach to accelerating materials innovation. *APL Mater.* **1**, 011002 (2013).
142. Jain, A. et al. Formation enthalpies by mixing GGA and GGA+U calculations. *Phys. Rev. B* **84**, 045115 (2011).
143. Song, S. W. et al. Study on anisotropy of n-type Mg_3Sb_2-based thermoelectric materials. *Appl. Phys. Lett.* **112**, 092103 (2018).
144. Li, J. et al. Computational prediction of a high ZT of n-type Mg_3Sb_2-based compounds with isotropic thermoelectric conduction performance. *Phys. Chem. Chem. Phys.* **20**, 7686–7693 (2018).
145. Grin, Y. Inhomogeneity and anisotropy of chemical bonding and thermoelectric properties of materials. *J. Solid State Chem.* **274**, 329–336 (2019).